Wave Dispersion Properties of Compound Finite Elements*

Thomas Melvin[1†] and J. Thuburn[2]

[1] Met Office, Exeter, U.K.
[2] University of Exeter, U.K.

30th January 2017

Abstract

Mixed finite elements use different approximation spaces for different dependent variables. Certain classes of mixed finite elements, called compatible finite elements, have been shown to exhibit a number of desirable properties for a numerical weather prediction model. In two-dimensions the lowest order element of the Raviart-Thomas based mixed element is the finite element equivalent of the widely used C-grid staggering, which is known to possess good wave dispersion properties, at least for quadrilateral grids. It has recently been proposed that building compound elements from a number of triangular Raviart-Thomas sub-elements, such that both the primal and (implied) dual grid are constructed from the same sub-elements, would allow greater flexibility in the use of different advection schemes along with the ability to build arbitrary polygonal elements. Although the wave dispersion properties of the triangular sub-elements are well understood, those of the compound elements are unknown. It would be useful to know how they compare with the non-compound elements and what properties of the triangular sub-grid elements are inherited?

Here a numerical dispersion analysis is presented for the linear shallow water equations in two dimensions discretised using the lowest order compound Raviart-Thomas finite elements on regular quadrilateral and hexagonal grids. It is found that, in comparison with the well known C-grid scheme, the compound elements exhibit a more isotropic dispersion relation, with a small over estimation of the frequency for short waves compared with the relatively large underestimation for the C-grid. On a quadrilateral grid the compound elements are found to differ from the non-compound Raviart-Thomas quadrilateral elements even for uniform elements, exhibiting the influence of the underlying sub-elements. This is shown to lead to small improvements in the accuracy of the dispersion relation: the compound quadrilateral element is slightly better for gravity waves but slightly worse for inertial waves than the standard lowest order Raviart-Thomas element.

KEYWORDS energy conservation; energy propagation; group velocity; numerical dispersion; mixed order elements

† Corresponding author: Met Office, FitzRoy Road, Exeter EX1 3PB, UK.
email: Thomas.Melvin@metoffice.gov.uk

1 Introduction

Traditionally most global atmospheric models used for numerical weather prediction have used a latitude-longitude grid for discretising the equations of motion, though increasingly many modelling groups now use (or are developing) some form of quasi-uniform grid. The latitude-longitude grid has many desirable properties such as orthogonality, symmetry and a logically rectangular structure. However, with the increasing number of processor cores expected in future generations of high performance computers, the communication bottleneck implied by the polar singularities in latitude-longitude grids has stimulated the interest in a range of quasi-uniform alternative grids and compact numerical methods. A number of quasi-uniform grids have proved popular in the atmospheric modelling community including: the cubed sphere, (e.g. Taylor and Fournier, 2010; Ullrich *et al.*, 2010); subdivision of the icosahedron using triangular (e.g. Majewski *et al.*, 2002) and hexagonal elements (e.g. Satoh *et al.*, 2008; Skamarock *et al.*, 2012; Gassmann, 2013).

A range of these quasi-uniform alternatives to the latitude-longitude grid for global atmospheric models is reviewed in Staniforth and Thuburn (2012). They listed a number of essential and desirable properties for an atmospheric model. These can be summarised as requiring the discretisation to: have good conservation properties; mimic certain continuous vector calculus identities; have an accurate representation of balance and adjustment; be free of unphysical modes (either through grid imprinting or computational modes); and have accuracy at least approaching second order.

Cotter and Shipton (2012) proposed a number of families of mixed finite elements for quasi-uniform horizontal grids (where mixed refers to the use of different function spaces for the dependent variables, see Auricchio *et al.*, 2004 for a review of mixed elements) which preserve a number of the desirable properties identified by Staniforth and Thuburn (2012). These methods rely upon defining appropriate function spaces $\mathbb{V}_i$ and operator mappings between the spaces. For example, in two dimensions:

$$\mathbb{V}_0 \underset{\mathbf{k}.\tilde{\nabla}\times}{\overset{\nabla^\perp}{\rightleftarrows}} \mathbb{V}_1 \underset{\tilde{\nabla}}{\overset{\nabla.}{\rightleftarrows}} \mathbb{V}_2, \tag{1}$$

where the $\nabla^\perp$ operator is $\boldsymbol{k} \times \nabla$, i.e. the rotation of the gradient operator by 90 degrees anticlockwise with unit vector $\mathbf{k}$ pointing out of the plane. The differential operators along solid lines map from $\mathbb{V}_i \rightarrow \mathbb{V}_{i+1}$ e.g. for a vector $\mathbf{w} \in \mathbb{V}_1$, then $\nabla.\mathbf{w} \in \mathbb{V}_2$. The differential operators along dashed lines map from $\mathbb{V}_i \rightarrow \mathbb{V}_{i-1}$ in the weak sense obtained via integration by parts, used in (17) and (25) below, for example the weak gradient operator $\tilde{\nabla}$ maps a scalar $\Phi \in \mathbb{V}_2$ to a vector $\tilde{\nabla}\Phi \in \mathbb{V}_1$ and is defined as $\int \boldsymbol{v}.\tilde{\nabla}\Phi da = \oint \boldsymbol{v}.\mathbf{n}\Phi dl - \int (\nabla.\boldsymbol{v})\,\Phi da$ for all $\boldsymbol{v} \in \mathbb{V}_1$. In a shallow water context the streamfunction and potential vorticity $\psi, q \in \mathbb{V}_0$, velocity $\mathbf{u} \in \mathbb{V}_1$ and geopotential $\Phi \in \mathbb{V}_2$. One particular family of finite element complexes suggested by Cotter and Shipton (2012) is the family of Raviart-Thomas elements (RT_k) (Raviart and Thomas, 1977) for velocity paired with a continuous bi-polynomial representation of scalars in $\mathbb{V}_0$ (Q_{k+1}) and a discontinuous bi-polynomial representation of scalars in $\mathbb{V}_2$ (Q_k^{DG}) denoted $Q_{k+1} - RT_k - Q_k^{DG}$, on quadrilaterals. The lowest order member of this family, $Q_1 - RT_0 - Q_0^{DG}$, corresponds to the mixed finite element analogue of the C-grid finite difference discretisation in that the same number and position of degrees of freedom is obtained. For triangular elements the polynomial space P_k is used instead of the tensor product space Q_k. At the lowest order both P_0^{DG} and Q_0^{DG} represent discontinuous fields that are constant within the element and can be used interchangeably. For notational simplicity the complex of functions spaces $Q_{k+1} - RT_k - Q_k^{DG}$ will be referred by only the vector space RT_k from here on.

At large scales atmospheric motion is dominated by balance and adjustment. Geostrophic and hydrostatic adjustment occur through the emission of inertia-gravity and acoustic waves and the discrete representation of balance can be analysed through the dispersion relation of the candidate numerical scheme. A C-grid staggering, where edge normal velocity components are staggered with respect to the mass variable is commonly used to achieve good dispersion properties, (Arakawa and Lamb, 1977). At lowest order compatible mixed finite elements can be viewed as the finite element generalisation of the C-grid staggering with the flexibility of using the finite element methodology to extend the discretisation to arbitrary order. Although using higher order elements improves the dispersion properties for a range of the spectrum, problems can arise, due to the increased number of branches of solutions, in the form of spectral gaps which can manifested themselves as trapped or distorted waves, for example in the RT_1 (Staniforth *et al.*, 2013) and spectral elements (Melvin *et al.*, 2012) methods. In a complete model of the atmosphere the physical parametrisations and boundary

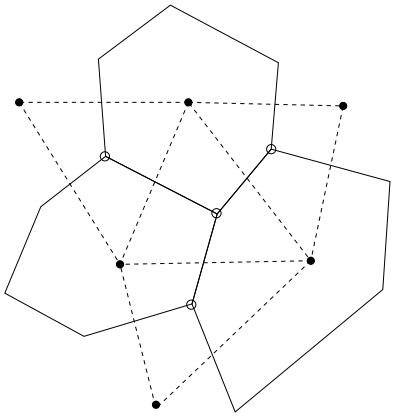

Figure 1: Primal (solid lines) and dual (dashed lines) grid where primal cell centres (filled circles) are dual vertices and dual cell centres (open circles) are primal vertices.

conditions can force at scales close the grid scale. Therefore, any unusual behaviour, even if near the limits of resolution, would be of concern. These problems can often be mitigated through various methods such as partial-mass lumping (Staniforth *et al.*, 2013), modified quadrature (Ullrich, 2014) or most commonly diffusion. The dispersion properties of a variety of other mixed elements was discussed by Le Roux (2012) (and references therein) to which the interested reader is referred for a more general discussion of mixed finite element dispersion properties. At the lowest order on quadrilaterals, there is a one-to-one mapping of analytical roots to the dispersion relation with the discrete branches (i.e. for the shallow water equations there are two inertia-gravity wave branches and one Rossby wave branch) and therefore spectral gaps are not a problem. However, on non-quadrilateral grids the C-grid staggering leads to a change in the ratio of velocity to mass degrees of freedom, such that there are either too many velocity degrees of freedom (as for a C-grid hexagon) or too many mass degrees of freedom (as for a C-grid triangle). This imbalance gives rise to spurious computational Rossby (Thuburn, 2008) or inertia-gravity (Danilov, 2010) modes respectively. At higher orders the mixed element approach allows the degree of freedom ratio to be chosen so as to retain the desired 2:1 ratio, (Cotter and Shipton, 2012), though this is not a sufficient requirement to obtain good dispersion properties.

A methodology for obtaining mimetic discretisations of the shallow water equations is presented by Cotter and Thuburn (2014) using finite element exterior calculus. They propose two methods: termed "primal" and "primal-dual" formulations. The "primal-dual" formulation of Cotter and Thuburn (2014) makes use of elements defined on both the primal and dual grid, Fig. 1, in addition to mappings between the corresponding function spaces. As noted in Cotter and Thuburn (2014) the use of a primal-dual formulation has the advantage over the primal only method of using the dual, discontinuous, representation of potential vorticity, therefore permitting the use of a wider range of discontinuous Galerkin/finite volume methods for computing vorticity fluxes. In order to construct the primal and dual grid elements we use a method proposed by Christiansen (2008) (extending the ideas of Buffa and Christiansen (2007)), which allows the primal and dual compound elements to be constructed out of the same set of sub-elements.

In addition this method also has the added benefit of providing a straightforward method for compound elements to be constructed for arbitrary polygons and this property will be used to construct a compound RT_0 element on a hexagonal mesh in addition to the compound RT_0 element on a quadrilateral mesh.

A comparison of the resultant compound elements, with both the C-grid finite difference and standard primal-only RT_0 elements on quadrilateral grids and with a C-grid finite difference scheme on a hexagonal grid (where there is no standard finite element formulation), will be the focus of this paper. Although the mimetic properties of the compound finite elements help to ensure that certain conservation and balance properties are well captured even on quasi-uniform meshes, they do not directly imply accurate wave dispersion. It is therefore important to check that their wave dispersion properties are at least as good as those of a C-grid. Investigation of the dispersion properties of the compound elements will be the particular focus of this paper; this provides useful insight into both the adjustment in response to imbalance and also the presence and behavior of any computational modes. Of particular interest is the group velocity, which governs the speed

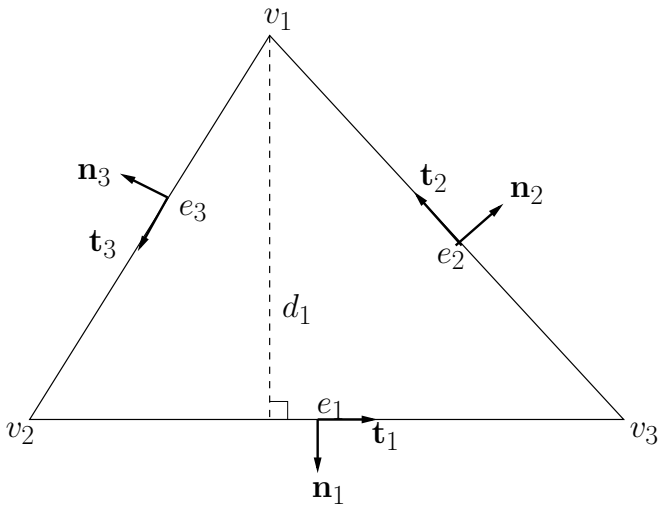

Figure 2: Triangular element with vertices ν_i, edges opposite vertices e_i of length l_i. Tangent and (outward) normal vectors to edge e_i are denoted $\mathbf{t}_i, \mathbf{n}_i$ respectively. d_i is the perpendicular distance from edge i to vertex i.

and direction of propagation of disturbances. It is well known that the C-grid discretisation slows down propagation such that the highest frequency resolved mode (the $2h$ wave, where h is the element width) has zero group velocity (c.f, a collocated A-grid discretisation where the $4h$ wave has zero group velocity and all waves with wavenumber $>2h$ have a group velocity with the wrong sign).

The rest of the paper is set out as follows. The $P_1 - RT_0 - P_0^{DG}$ finite element space on triangular elements is reviewed in Section 2. Section 3 describes how the compound elements are formed from the sub-elements and formulates the basis functions on the compound element. The discrete linear shallow water equations are formed in Section 4 for uniform elements. The dispersion properties of the compound elements are investigated in Section 5 and compared with the well known C-grid finite difference and standard RT_0 discretisations. Numerical simulations are performed in Section 6 to confirm some of the theoretical properties derived earlier, and finally conclusions are drawn in Section 7.

2 $P_1 - RT_0 - P_0^{DG}$ Triangular elements

The $P_1 - RT_0 - P_0^{DG}$ triangular elements have two function spaces for scalars (P_1 and P_0^{DG}) and one for vectors (RT_0). The P_1 space contains scalars that vary linearly within each element and are continuous between elements, there are three degrees of freedom per element located at the element vertices and shared between all elements that share the vertex. Vectors have continuous normal components at element edges (with a constant normal component along the edge), within the element the vector field varies linearly and is curl free. As a result of this the tangential components are discontinuous at element edges. There are three degrees of freedom per element for a vector field, one per edge, which are shared with elements that share the edge. The P_0^{DG} space contains scalars that have a piecewise constant representation and one scalar degree of freedom per element. The location of degrees of freedom is therefore the same as for a triangular C-grid discretisation. For the shallow water equations this results in a 3:2 velocity to height degree of freedom ratio and therefore the triangular based RT_0 discretisation suffers from the same computational inertia-gravity wave mode as the C-grid (Danilov, 2010; Le Roux, 2012).

Consider the triangular element as shown in Fig. 2 with vertices ν_i located at (x_i, y_i). The barycentric coordinates of a point $\mathbf{x} = (x, y)$ are given by $\boldsymbol{\lambda} = (\lambda_1, \lambda_2, \lambda_3)$ where $\lambda_j = 1$ at vertex $i = j$ and $\lambda_j = 0$ at vertex $i \neq j$, see Coxeter (1989) for details. The basis functions used to construct the RT_0 elements consist of: piecewise linear functions in space $\mathbb{V}_0$ that are continuous between elements

$$\chi_i(x, y) \equiv \lambda_i(x, y), \tag{2}$$

$\nabla\chi_i(x,y) \equiv \nabla\lambda_i(x,y) = -\frac{\mathbf{n}_i}{d_i}$
$\nabla.\mathbf{w}_i(x,y) = 2 \equiv 2\rho(x,y)$
$\mathbf{k}.\nabla \times \mathbf{w}(x,y)_i = 0$
$\nabla^{\perp}\chi_i(x,y) = -\frac{\mathbf{t}_i}{d_i} \equiv \frac{\mathbf{w}_k(x,y)-\mathbf{w}_j(x,y)}{l_i d_i}$

Table 1: Useful relationships of the triangular $P1-RT0-P0$ basis functions.

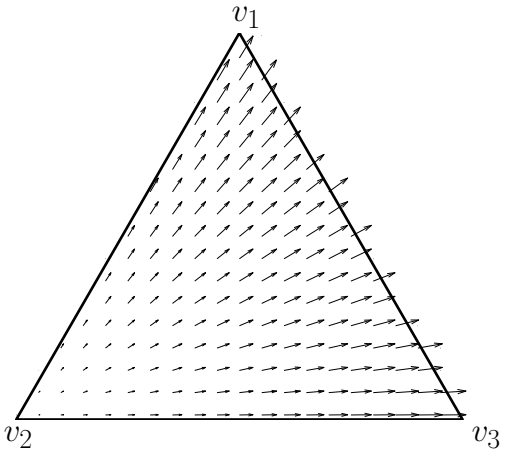

Figure 3: Basis function $\mathbf{w}_2$ for a triangular RT_0 element associated with edge 2 as described in Fig. 2.

where $i = 1,2,3$ indicates which vertex of the element χ_i is associated with; vectors with constant normal components along edges in $\mathbb{V}_1$

$$\mathbf{w}_i(x,y) \equiv \lambda_j(x,y)\, l_k \mathbf{t}_k - \lambda_k(x,y)\, l_j \mathbf{t}_j, \tag{3}$$

where $i = 1,2,3$ and j and k are cyclic increments of i and j respectively, as an example $\mathbf{w}_2$ is shown in Fig.3; and piecewise constant functions in the function space $\mathbb{V}_2$

$$\rho(x,y) \equiv 1. \tag{4}$$

Variables in each function space can be expressed as weighted sums of the appropriate basis functions. Some useful properties of the basis functions that will be needed in the following sections are given in Table 1.

3 Compound RT_0 elements

The compound elements are constructed by first subdividing the polygonal element into a number of smaller sub-elements. The number and shape of the sub-elements is constrained by the need to consistently build both the primal and dual grid out of the same set of sub-elements and therefore the overlap area between the primal and dual grid needs to be exactly divided into a number of sub-elements. For a polygonal grid the primal-dual overlap is a quadrilateral, in the form of a kite. Therefore, the sub-elements are required to be either triangles (by further subdividing the kite) or quadrilaterals. Since any polygonal shape can be divided into triangles, and triangles are also convenient for approximating curved surfaces (such as the sphere) by planar facets, this choice of sub-elements offers greater flexibility for future implementation on nonuniform grids, see Fig. 4. For example, although a hexagon could be sub-divided into only six triangles by joining each vertex to the centre of the element, this would be inconsistent with the corresponding subdivision of the dual element triangle, which would be subdivided into three smaller triangles through joining each vertex to the centre of the dual element.

To construct the basis functions for the compound elements we use the harmonic extension ideas of Christiansen (2008). We wish to construct the compound element function spaces $\mathbb{V}_0^{(C)}$, $\mathbb{V}_1^{(C)}$, $\mathbb{V}_2^{(C)}$ out of the larger spaces of the sub-element function spaces $\mathbb{V}_0$, $\mathbb{V}_1$, $\mathbb{V}_2$. For example, to construct a basis function,

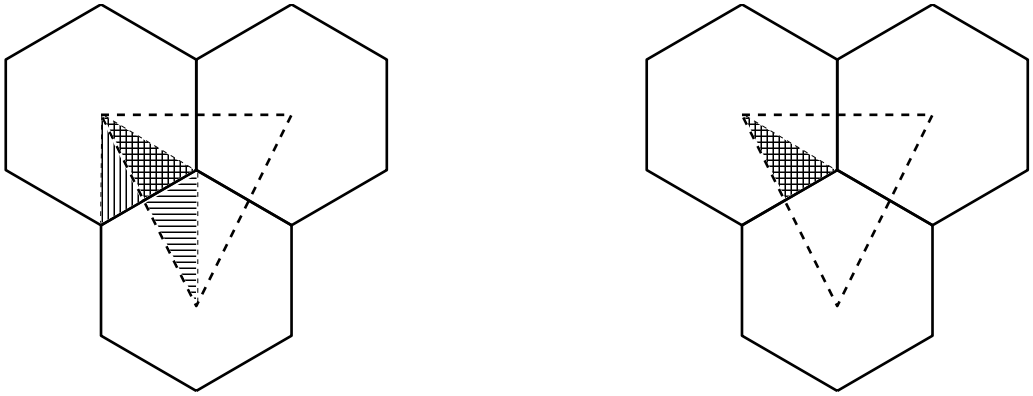

(a) (b)

Figure 4: Subdivision of the primal-hexagonal and dual-triangular grids using (a) inconsistent subdivision (the sub-elements on the primal and dual grid are not identical) with 6 sub-elements for the primal-hexagonal compound elements, indicated by vertical shading and 3 sub-elements for the dual-triangular compound elements, indicated by horizontal shading and (b) consistent subdivision (the sub-elements on the primal and dual grid are identical) using 12 sub-elements for the primal-hexagonal compound elements and 6 sub-elements for the dual compound-triangular elements.

$\mathbf{w} \in \mathbb{V}_1^{(C)}$, where the superscript denotes application to the constructed compound element, first boundary conditions are imposed, namely that the normal component of $\mathbf{w}$ is nonzero and constant only along one edge of the polygonal element. Then the basis function is extended harmonically into the interior of the element, that is, to satisfy

$$\nabla\left(\nabla.\mathbf{w}\right) \equiv 0, \tag{5}$$

$$\mathbf{k}.\nabla\times\mathbf{w} \equiv 0. \tag{6}$$

Similar constructions hold for basis functions in other spaces. Unfortunately exact solutions of (5) and (6) do not generally have analytic expressions. However, a discrete version of (5) and (6) can be solved by dividing each polygonal element into triangular sub elements and using an RT_0 finite element discretisation on the space of sub-elements, thus giving a discrete harmonic extension. Moreover, it can be shown that the function spaces obtained in this way are compatible (Christiansen, 2008).

Consider a compound element made up of n triangular sub-elements T_i, $i = 1,..,n$, where $n = 8$ for a compound quadrilateral element and $n = 12$ for a compound hexagonal element, Fig. 5. A variable is expanded in terms of compound basis functions in the same way as for a non-compound element but with time dependent coefficients located as in Fig 6. Hence for variables in the compound function spaces $\mathbb{V}_i^{(C)}$that we wish to construct: $(\psi,\, \mathbf{u},\, \Phi) \in \left(\mathbb{V}_0^{(C)},\, \mathbb{V}_1^{(C)},\, \mathbb{V}_2^{(C)}\right)$ the expansions are

$$\psi\left(\mathbf{x},t\right) = \sum_{k=1}^{nvert} \psi_k\left(t\right)\chi_k^{(C)}\left(\mathbf{x}\right), \tag{7}$$

$$\mathbf{u}\left(\mathbf{x},t\right) = \sum_{k=1}^{nedge} u_k\left(t\right)\mathbf{w}_k^{(C)}\left(\mathbf{x}\right), \tag{8}$$

$$\Phi\left(\mathbf{x},t\right) = \Phi\left(t\right)\rho^{(C)}\left(\mathbf{x}\right), \tag{9}$$

where $\left(\chi_k^{(C)},\, \mathbf{w}_k^{(C)},\, \rho^{(C)}\right)$ are the compound basis functions and *nvert* and *nedge* are the number of external vertices and edges on the compound element respectively, i.e. both *nvert* and *nedge* are 4 for a quadrilateral

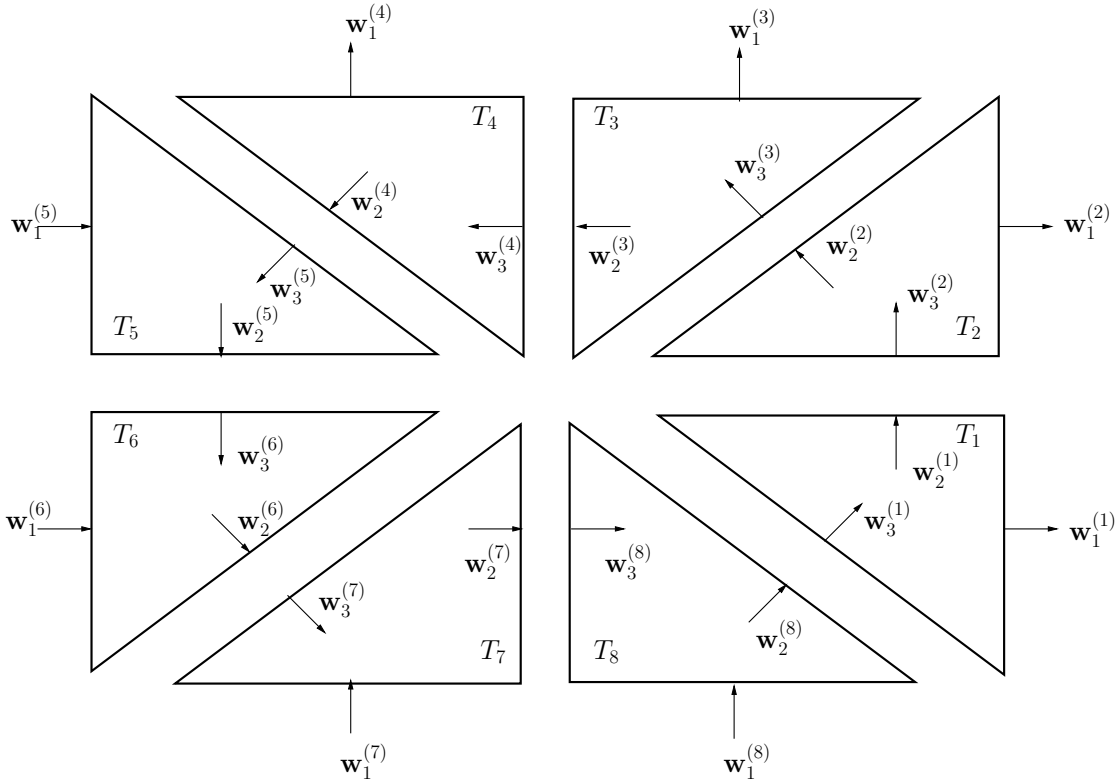

(a)

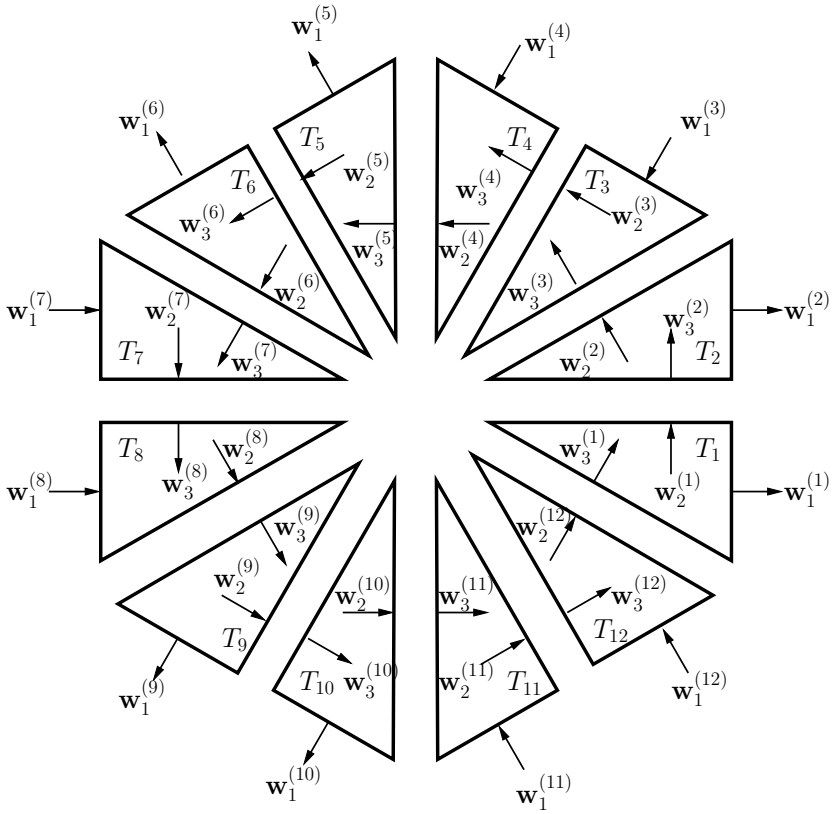

(b)

Figure 5: (a) Quadrilateral element made up of 8 triangular RT_0 elements, $T_1, .., T_8$, the compound element is formed by gluing the sub-elements together. Arrows indicate locations of the velocity basis functions $\mathbf{w}_i^{(j)}$ associated with each sub-element j. (b) Similar construction can be made for a compound hexagonal element using 12 triangular RT_0 elements. Note the convention that edge 1 of the sub-element is on the outer edge of the compound element.

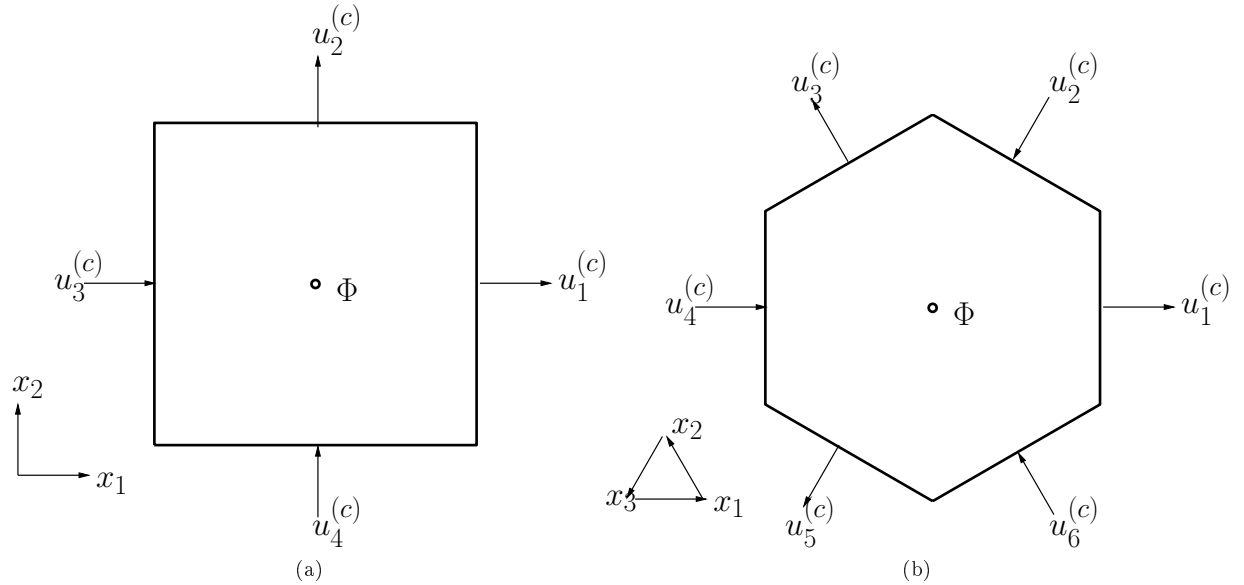

Figure 6: Location of velocity and geopotential degrees of freedom on the compound elements for (a) quadrilaterals and (b) hexagons.

or 6 for a hexagon. The compound basis functions are then written as a linear combination of the sub-element basis functions

$$\chi_k^{(C)}(\mathbf{x}) = \sum_{j=1}^{n} \sum_{i=1}^{nvert_s} \alpha_i^{(j)} \chi_i^{(j)}(\mathbf{x}), \tag{10}$$

$$\mathbf{w}^{(C)}(\mathbf{x}) = \sum_{j=1}^{n} \sum_{i=1}^{nedge_s} \beta_i^{(j)} \mathbf{w}_i^{(j)}(\mathbf{x}), \tag{11}$$

$$\rho^{(C)}(\mathbf{x}) = \sum_{j=1}^{n} \gamma^{(j)} \rho^{(j)}(\mathbf{x}), \tag{12}$$

where n is the number of sub-elements, and $nvert_s$ and $nedge_s$ are the number of vertices and edges on a sub-element, which for the triangles used here are always 3, (see Fig. 5 for locations of the $\mathbf{w}_i^{(j)}$sub-element basis functions). For the right hand side sub-element terms the superscript refers to the sub-element index and the subscript refers to the edge or vertex of the sub-element which follows the convention that edge 1 lies on the edge of the compound element and the edge index increases in the anticlockwise direction, and vertex i is opposite edge i. The sub-element basis functions $\psi_i^{(j)}$, $\mathbf{w}_i^{(j)}$ and $\rho^{(j)}$ take their usual value inside sub-element j and are zero outside of it. It remains then to find the coefficients α, β and γ for each compound basis function, this is done through imposing discrete versions of (5) and (6) along with boundary conditions.

For a $\mathbb{V}_2$ field each sub-element (j) has a constant value $\rho^{(j)}$, therefore to ensure the compound element basis function is continuous across sub-element boundaries requires

$$\gamma^{(j)} \equiv const = 1, \forall j = 1, .., n. \tag{13}$$

Therefore compound basis function, $\rho^{(C)} = 1$ is constant throughout the compound element, as for a standard non-compound RT_0 element.

To form the compound $\mathbb{V}_1$ basis functions three sets of constraints are applied. First, the normal flux along each edge of the compound element is required to be continuous and constant, requiring

$$\beta_1^{(i)} d_i = \beta_1^{(j)} d_j = 0, \; or \; const, \tag{14}$$

where $\beta_1^{(i)}$, $\beta_1^{(j)}$ are the coefficients of the expansion (11) along a compound element edge, and d_i, d_j are the perpendicular distances from the corresponding vertices to the edges of the sub-element. For a compound basis function $\mathbf{w}_k^{(c)}$ then $\beta_1^{(i)} d_i = const$ if edge 1 of sub-element i is a section of compound edge k and $\beta_1^{(i)} d_i = 0$ otherwise, (see caption of Fig. 5) . Second, mimicking the non-compound element, the divergence within the compound element is required to be constant, this is equivalent to enforcing (5). Using Table 1 and (11) this can be expressed as

$$\sum_{i=1}^{3} s_i^{(j)} \beta_i^{(j)}(t) = \sum_{i=1}^{3} s_i^{(k)} \beta_i^{(k)}(t), \qquad \forall j,k = 1,..,n, \tag{15}$$

with $s_i^{(j)} = \pm 1$ being the sign of $\nabla.\mathbf{w}_i^{(j)}$. The final constraint on the $\mathbb{V}_1$ basis is that, mimicking $\boldsymbol{k}.\nabla\times\boldsymbol{w} = 0$, and equivalent to enforcing (6), a measure of vorticity is required to vanish inside the compound element. The vorticity is given by $\xi = \mathbf{k}.\nabla \times \mathbf{w}^{(C)}$. However the curl of the velocity is not defined and so the weak form of the vorticity is used and it is demanded that this weak formulation of vorticity vanishes inside the compound element. For a test function $\chi \in \mathbb{V}_0$ (note that $\chi \notin \mathbb{V}_0^{(C)}$ for the compound element function space $\mathbb{V}_0^{(C)}$ which is a subset of $\mathbb{V}_0$) the constraint that an integrated measure of the vorticity vanishes over the compound element e_c, can be expressed as

$$\int_{e_c} \chi \xi ds \equiv \int_{e_c} \chi \left(\mathbf{k}.\tilde{\nabla} \times \mathbf{w}^{(C)} \right) ds = 0. \tag{16}$$

Evaluating the curl in the weak sense by integrating by parts this becomes

$$-\int_{e_c} \nabla^{\perp}\chi.\mathbf{w}^{(C)} ds = 0. \tag{17}$$

Taking χ located at the centre of the compound element, yields, using Table 1

$$-\sum_{j=1}^{n} \int_{T_j} \nabla^{\perp}\chi. \sum_{i=1}^{3} \left(\beta_i^{(j)} \mathbf{w}_i^{(j)} \right) ds = \sum_{j=1}^{n} \int_{T_j} \frac{\mathbf{t}_1^{(j)}}{d_1^{(j)}}. \sum_{i=1}^{3} \left(\beta_i^{(j)} \mathbf{w}_i^{(j)} \right) ds = 0, \tag{18}$$

where $\mathbf{t}_1^{(j)}$ is the tangent vector to the edge of sub-element j lying on the boundary of the compound element. Using (14), (15) and (18) the values of β can be determined for each compound basis function. Note that when the compound elements are constructed in this way, (1) holds for $\mathbb{V}_0^{(C)}$, $\mathbb{V}_1^{(C)}$, $\mathbb{V}_2^{(C)}$,

For the quadrilateral element in Fig 5 (a) the compound velocity basis function associated with edge 1, Fig 6 (a), is:

$$\begin{aligned} \mathbf{w}_1^{(C)} d_1^{(C)} \equiv \frac{1}{4} \Big[& \left(3\mathbf{w}_2^{(8)} - 2\mathbf{w}_3^{(8)} \right) + \left(4\mathbf{w}_1^{(1)} - 3\mathbf{w}_3^{(1)} \right) + \left(4\mathbf{w}_1^{(2)} - 3\mathbf{w}_2^{(2)} \right) + \left(3\mathbf{w}_3^{(3)} - 2\mathbf{w}_2^{(3)} \right) \\ & + \left(2\mathbf{w}_3^{(4)} - \mathbf{w}_2^{(4)} \right) + \left(\mathbf{w}_3^{(5)} \right) + \left(\mathbf{w}_2^{(6)} \right) + \left(2\mathbf{w}_2^{(7)} - \mathbf{w}_3^{(7)} \right) \Big], \end{aligned} \tag{19}$$

where $d_1^{(C)}$ is the perpendicular distance from the compound edge 1 to the center of the element, i.e. half the element width. The other compound basis functions, $\mathbf{w}_j^{(C)}, j = 2,..,4$, can be obtained in sequence from $\mathbf{w}_k^{(C)}, k = 1,..,3$ by increasing the sub-element index by 2 (modulo 8) and multiplying by -1. In addition a normalisation has been applied so that for a unit element $\mathbf{w}_j^{(C)}.\mathbf{n}_j^{(C)} = 1$ along edge j. Fig. 7 (a) shows $\mathbf{w}_1^{(C)}$ in the compound element. Note, that even for a uniform compound element on a plane, as considered here, this results in a considerably different set of basis functions to the non-compound RT_0 element on a quadrilateral where the equivalent to (19) would be

$$\mathbf{w}_1^{\text{quad}} \equiv \frac{(x - x^-)}{x^+ - x^-}\mathbf{i}, \tag{20}$$

where x^+ and x^- indicate the positions of the right- and left-hand edges of the element respectively.

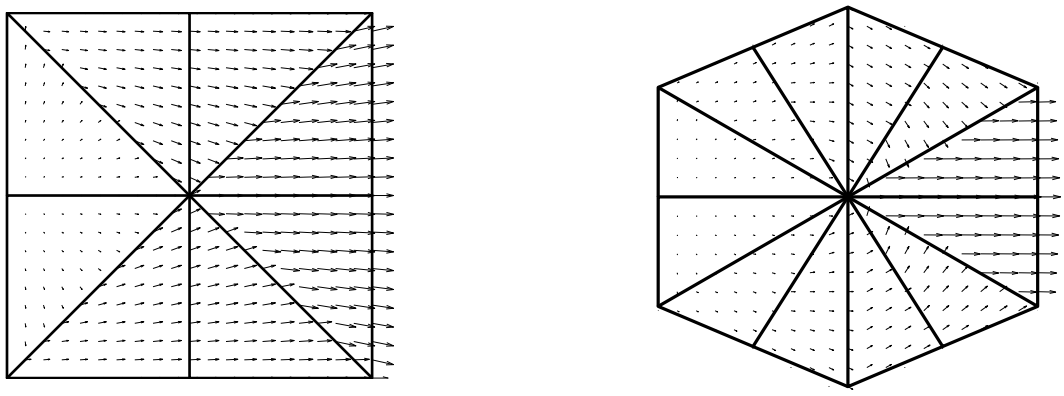

(a) (b)

Figure 7: Compound basis functions for a (a) compound quadrilateral (19), and (b) compound hexagon (21).

For the hexagonal element in Fig. 5 (b) the compound basis function associated with edge 1, Fig 6 (b), is:

$$\begin{aligned}\mathbf{w}_1^{(C)} d_1^{(C)} \quad = \quad & \frac{1}{6}\Big[\left(6\mathbf{w}_1^{(1)} - 5\mathbf{w}_3^{(1)}\right) + \left(6\mathbf{w}_1^{(2)} - 5\mathbf{w}_2^{(2)}\right) + \left(5\mathbf{w}_3^{(3)} - 4\mathbf{w}_2^{(3)}\right) + \left(4\mathbf{w}_3^{(4)} - 3\mathbf{w}_2^{(4)}\right) \\ & + \left(3\mathbf{w}_3^{(5)} - 2\mathbf{w}_2^{(5)}\right) + \left(2\mathbf{w}_3^{(6)} - \mathbf{w}_2^{(6)}\right) + \left(\mathbf{w}_3^{(7)}\right) + \left(\mathbf{w}_2^{(8)}\right) + \left(2\mathbf{w}_2^{(9)} - \mathbf{w}_3^{(9)}\right) \\ & + \left(3\mathbf{w}_2^{(10)} - 2\mathbf{w}_3^{(10)}\right) + \left(4\mathbf{w}_2^{(11)} - 3\mathbf{w}_3^{(11)}\right) + \left(5\mathbf{w}_2^{(12)} - 4\mathbf{w}_3^{(12)}\right)\Big],\end{aligned} \tag{21}$$

and $\mathbf{w}_j^{(C)}, j = 2, .., 6$ can again be obtained in sequence from $\mathbf{w}_k^{(C)}, k = 1, .., 5$ by increasing the sub-element index by 2 (modulo 12) and multiplying by -1 and the same normalisation as used for the quadrilateral elements has been applied. Fig. 7 (b) shows $\mathbf{w}_1^{(C)}$ in a hexagonal compound element.

In principle the preceding method could be applied to create a primal grid made of compound triangular elements (where each compound triangle is subdivided into six sub-elements), however, applying the constraints in this section, the resulting compound element, for a uniform subdivision, inherits the same basis functions and hence dispersion properties as the non-compound triangular RT_0 element that was analysed by Le Roux *et al.* (2008); Le Roux (2012).

It is worth noting that for regular geometry it is possible to form the compound elements by hand, however, for a more general geometry this would be very time consuming and would not be recommended, instead it is suggested to apply the constraints numerically.

For the linear shallow water equations considered here the compound $\mathbb{V}_0^{(C)}$ field is not needed and so the computations for the compound basis functions $\chi^{(C)}$ are omitted, though the process for computing them follows a similar method to the $\mathbb{V}_1^{(c)}$ and $\mathbb{V}_2^{(c)}$ fields.

4 Discrete equations

The 2D continuous linear shallow water equations on an $f-$plane are

$$\frac{\partial \Phi}{\partial t} + \Phi_0 \nabla . \mathbf{u} = 0, \tag{22}$$

$$\frac{\partial \mathbf{u}}{\partial t} + \nabla \Phi + f\mathbf{u}^{\perp} = 0, \tag{23}$$

with constant reference geopotential Φ_0. Rewriting these in the weak form, introducing test functions ρ and $\mathbf{w}$ in the geopotential and velocity space respectively and integrating over a domain $\Omega \in \mathbb{R}^2$ yields

$$\int_\Omega \rho \frac{\partial \Phi}{\partial t} da + \Phi_0 \int_\Omega \rho \nabla . \mathbf{u} da = 0, \tag{24}$$

$$\int_\Omega \mathbf{w} . \frac{\partial \mathbf{u}}{\partial t} da - \int_\Omega \Phi \nabla . \mathbf{w} da + \int_\Omega f \mathbf{w} . \mathbf{u}^\perp da = 0, \tag{25}$$

where the $\nabla\Phi$ term in (25) is evaluated in the weak sense and has been integrated by parts where periodic boundary conditions have been assumed. Substituting (8) and (9) into (24) and (25) and integrating over the compound elements gives the element-wise discrete equations. The spatially discrete equations are written in matrix-vector form as a sum over each element-wise discrete equation, which are

$$\sum_e M_\Phi \frac{\partial \hat{\Phi}^{(e)}}{\partial t} + \Phi_0 D \hat{u}^{(e)} = 0, \tag{26}$$

and

$$\sum_e M_u \frac{\partial \hat{u}^{(e)}}{\partial t} - D^T \hat{\Phi}^{(e)} + F \hat{u}^{(e)} = 0, \tag{27}$$

for the continuity and momentum equations respectively. $\hat{\Phi}^{(e)}$ and $\hat{u}^{(e)}$ are the vectors of geopotential and velocity degrees of freedom for element e respectively. Each compound element e has a single geopotential degree of freedom associated with it, and either 4 (for quads) or 6 (for hexagons) velocity degrees of freedom. The element degree of freedom vectors are therefore.

$$\hat{\Phi}^{(e)} \equiv [\Phi], \tag{28}$$

$$\hat{u}^{(e)}_{\text{quad}} \equiv \left[\begin{array}{cccc} u^+, & u^-, & v^+, & v^- \end{array} \right]^T, \tag{29}$$

$$\hat{u}^{(e)}_{\text{hex}} \equiv \left[\begin{array}{cccccc} u^+, & u^-, & v^+, & v^-, & w^+, & w^- \end{array} \right]^T. \tag{30}$$

The velocity components u, v, w point in the x_1, x_2, x_3 directions respectively (see (37) & (46) below) and the superscripts indicate whether the component points out of (+) or into (−) the element. In addition there is a 1-1 mapping between these components and $u_j^{(c)}$ as used in Fig. 6 given by

$$\left[u^+, u^-, v^+, v^-\right] \equiv \left[u_1^{(c)}, u_3^{(c)}, u_2^{(c)}, u_4^{(c)}\right] \tag{31}$$

$$\left[u^+, u^-, v^+, v^-, w^+, w^-\right] \equiv \left[u_1^{(c)}, u_4^{(c)}, u_2^{(c)}, u_5^{(c)}, u_3^{(c)}, u_6^{(c)}\right] \tag{32}$$

for quadrilaterals and hexagons respectively. In addition: M_u and M_Φ are the mass matrices; D is the matrix associated with the divergence operator; its transpose D^T is the matrix associated with the gradient operator and F is the operator associated with $f\mathbf{k}\times$. These are given for uniform elements of width h in Appendix A. Note that the resulting operator matrices for both a C-grid finite difference and an RT_0 based discretisation (using both compound and, on quadrilaterals, regular basis functions) differ only in the velocity mass matrix M_u. This is true for both the quadrilateral and hexagonal based methods. See Appendix A for details.

5 Dispersion Analysis

The discrete dispersion relation for both quadrilateral and hexagonal compound elements using the same methodology as Thuburn (2008) and Staniforth *et al.* (2013) is adopted. Begin by seeking solutions of the form

$$\Phi = P \exp\left[i\left(\mathbf{k}.\mathbf{x} - \omega t\right)\right], \tag{33}$$

$$u^\pm = U \exp\left[i\left(\mathbf{k}.\mathbf{x} - \omega t\right)\right], \tag{34}$$

$$v^\pm = V \exp\left[i\left(\mathbf{k}.\mathbf{x} - \omega t\right)\right], \tag{35}$$

$$w^\pm = W \exp\left[i\left(\mathbf{k}.\mathbf{x} - \omega t\right)\right], \tag{36}$$

with $\mathbf{x} \equiv (x, y)$, $\mathbf{k} \equiv (k, l)$.

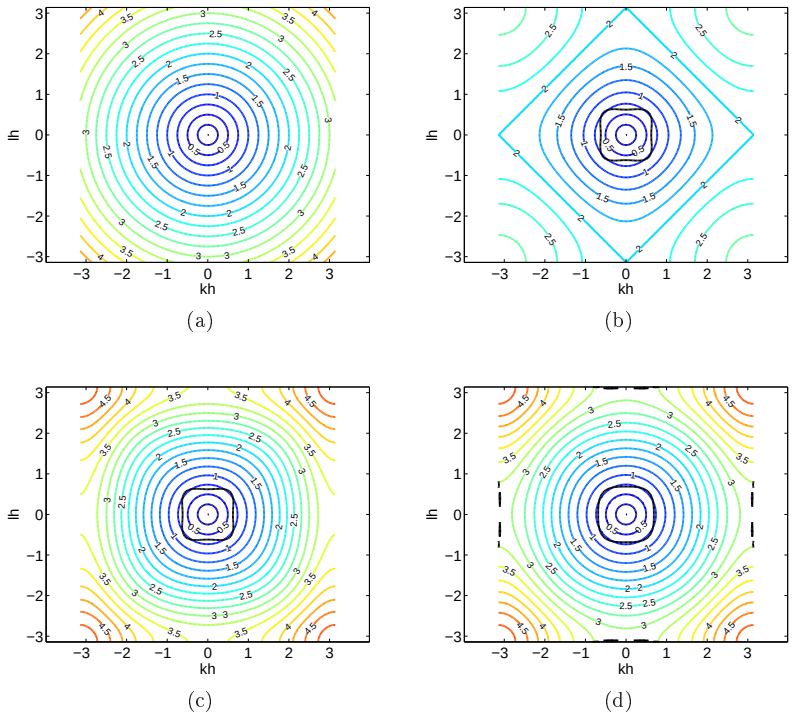

Figure 8: Normalised $\left(\omega h/\sqrt{\Phi_0}\right)$ dispersion relation for gravity-wave equations, ($f \equiv 0$): (a) Exact solution, (b) C-grid finite difference, (c) standard quadrilateral RT_0 element and (d) compound quadrilateral RT_0 element. Contour interval 0.25. Solid black contour shows the effective resolution, the region within which the dispersion relation error $\leq 1\%$.

5.1 Quadrilateral Elements

It is convenient to work in terms of coordinate directions normal to element edges, therefore, for quadrilateral elements define

$$(x_1, x_2) \equiv (x, y)\,, \tag{37}$$

$$(k_1, k_2) \equiv (k, l)\,. \tag{38}$$

Substituting (33)-(35) into (26) and (27) with the mass matrix M_u as given in Appendix A (A.4) for the compound elements and using (37)-(38) gives

$$-\omega P + 2\frac{\Phi_0}{h}\left[S_1 U + S_2 V\right] = 0, \tag{39}$$

$$-\frac{1}{12}\omega\left(\left[7C_1^2+5\right]U - S_2 S_1 V\right) + 2S_1\frac{P}{h} + ifC_1C_2V = 0, \tag{40}$$

$$-\frac{1}{12}\omega\left(\left[7C_2^2+5\right]V - S_1 S_2 U\right) + 2S_2\frac{P}{h} - ifC_1C_2U = 0 \tag{41}$$

with $S_j \equiv \sin\left(k_j h/2\right)$ and $C_j \equiv \cos\left(k_j h/2\right)$ with $j = 1, 2$. Writing this in matrix form results in

$$\begin{bmatrix} -\omega & 2\frac{\Phi_0}{h}S_1 & 2\frac{\Phi_0}{h}S_2 \\ \frac{2S_1}{h} & -\frac{1}{12}\omega\left(7C_1^2+5\right) & \frac{1}{12}\omega S_1 S_2 + ifC_1C_2 \\ \frac{2S_2}{h} & \frac{1}{12}\omega S_1 S_2 - ifC_1C_2 & -\frac{1}{12}\omega\left(7C_2^2+5\right) \end{bmatrix} \begin{bmatrix} P \\ U \\ V \end{bmatrix} = \mathbf{0}, \tag{42}$$

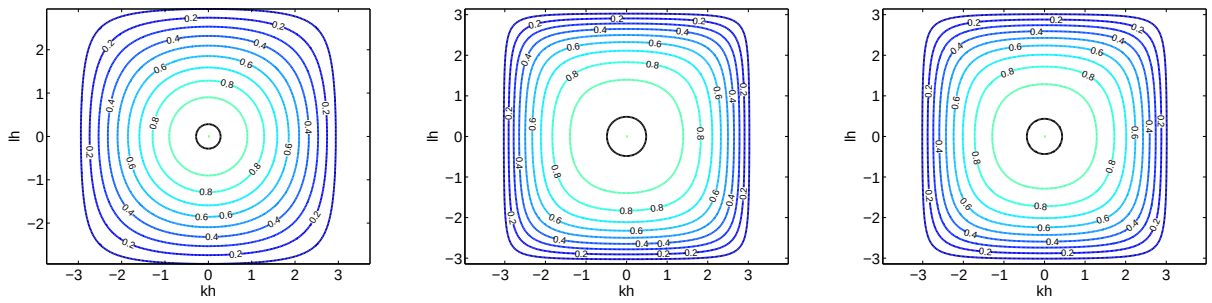

(a) (b) (c)

Figure 9: Normalised (ω/f) dispersion relation for inertia-wave equations ($\Phi_0 \equiv 0$): (a) C-grid finite difference, (b) standard quadrilateral RT_0 element and (c) compound quadrilateral RT_0 element. Contour interval 0.1. Solid black contour shows the effective resolution, the region within which the dispersion relation error $\leq 1\%$..

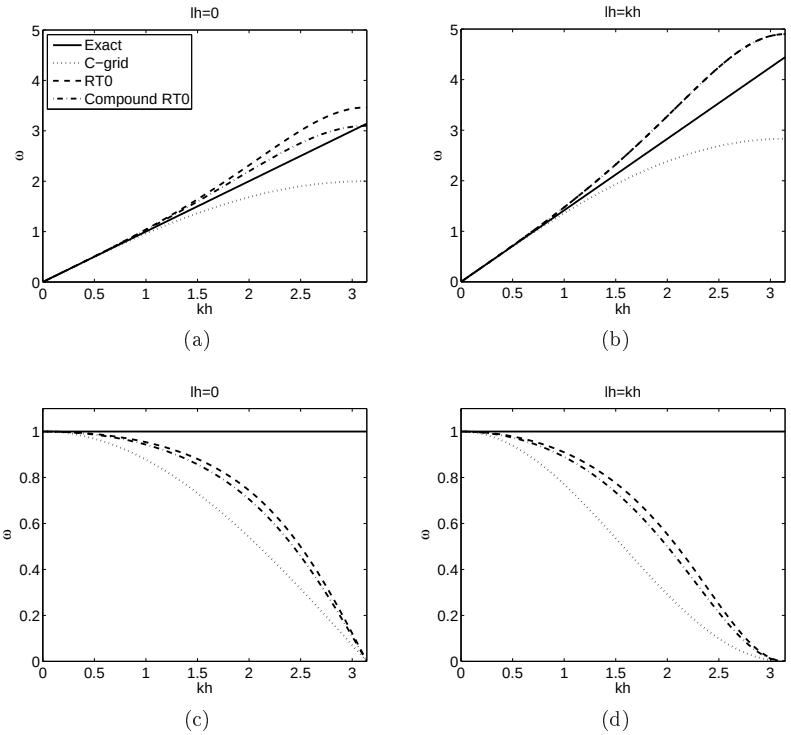

(a) (b)

(c) (d)

Figure 10: Quadrilateral elements: (a) & (c) Centroid-edge ($lh = 0$) and (b) & (d) Centroid-node ($kh = lh$) cross-sections of the gravity wave (a-b) and inertia-wave (c-d) limits.

yielding the dispersion relation

$$\omega\left\{-\left(\frac{\omega}{12}\right)^2\left[\left(7C_2^2+5\right)\left(7C_1^2+5\right)-S_2^2S_1^2\right]+f^2C_1^2C_2^2+\frac{1}{3}\frac{\Phi_0}{h^2}\left[S_2^2\left(7C_1^2+5+S_1^2\right)+S_1^2\left(7C_2^2+5+S_2^2\right)\right]\right\}=0 \tag{43}$$

which has solutions:

$$\omega=0,\pm 12\sqrt{\frac{\frac{1}{3}\frac{\Phi_0}{h^2}\left[S_2^2\left(S_1^2+7C_1^2+5\right)+S_1^2\left(S_2^2+7C_2^2+5\right)\right]+f^2C_1^2C_2^2}{\left[\left(7C_2^2+5\right)\left(7C_1^2+5\right)-S_2^2S_1^2\right]}}. \tag{44}$$

Note the presence of the $\omega=0$ root is guaranteed by the mimetic properties of the scheme, even on non-regular meshes. For small (kh,lh) it can be verified that

$$\omega\sim 0,\pm\left\{\omega_0+\frac{1}{96\omega_0}\left[3\Phi_0\left(k^4+l^4\right)+2\Phi_0k^2l^2-5f^2\left(k^2+l^2\right)\right]h^2+O\left(h^4\right)\right\}, \tag{45}$$

with $\omega_0=\sqrt{\Phi_0\left(k^2+l^2\right)+f^2}$, providing a useful check on the correctness of (44) and showing that scheme is second order accurate on the regular grid used here.

For pure gravity waves ($f\equiv 0$) the positive non-zero root of (44) is shown in Fig. 8 (d) along with the (a) exact, (b) C-grid finite difference and (c) non-compound RT_0 quadrilateral element results for comparison. The compound element, panel (d), can be seen to improve upon the isotropy of the dispersion relation compared with both the C-grid, panel (b), and the non-compound RT_0 element, panel (c) at least for small k. For pure inertia waves ($\Phi_0\equiv 0$) the positive non-zero root of (44) is shown in Fig. 9, again along with the C-grid finite difference and non-compound RT_0 quadrilateral element results for comparison. In this case the exact solution is unity and is therefore omitted. Here, all three methods produce very similar results, although frequency for the RT_0 elements drops off more slowly than the C-grid method. Cross-sections of Figs 8 and 9 along centroid-edge and centroid-node slices are shown in Fig 10. The centroid-edge slices (panels (a) and (c)) are the dispersion relations that would be obtained for a 1d model. For gravity waves the compound element reduces the overestimation of the frequency, increasing the accuracy for large wavenumbers. This result is partially reversed for inertia waves where underestimation of the frequency in the standard RT_0 element is made worse in the compound method. The centroid-node slices show that for gravity waves (panel (b)) the standard and compound elements produce the same overestimation of the frequency whilst for inertia waves (panel (d)) the compound element again increases the underestimation of the of frequency slightly when compared to the standard elements.

The x-component of the group velocity $\partial\omega/\partial k$ for the gravity wave equation is shown in Fig. 11. Both RT_0 methods exhibit overshoots in the group velocity, although the overshoot is greatly reduced for the compound element, $\mathrm{Max}\left(C_g\right)\approx 1.2$ at $(kh,lh)=\left(2\mathrm{atan}\left(3/\sqrt{5}\right),0\right)$, compared to the standard element, $\mathrm{Max}\left(C_g\right)\approx 1.4$ at $(kh,lh)=(2\pi/3,0)$. Due to symmetry the same maximum values are found for the y component if kh and lh are swapped. It should be noted that $C_g\longrightarrow 0$ at $k=k_{max}$ for all three schemes.

5.2 Hexagonal Elements

As before it is convenient to work in terms of directions normal to element edges and so for hexagonal elements

$$(x_1,x_2,x_3)\equiv\left(x,-\frac{1}{2}x+\frac{\sqrt{3}}{2}y,-\frac{1}{2}x-\frac{\sqrt{3}}{2}y\right), \tag{46}$$

$$(k_1,k_2,k_3)\equiv\left(k,-\frac{1}{2}k+\frac{\sqrt{3}}{2}l,-\frac{1}{2}k-\frac{\sqrt{3}}{2}l\right). \tag{47}$$

Substituting (33)-(36) into (26)-(27) with the mass matrix M_u from the compound elements and using (46)-(47) yields

$$-\omega P+\frac{4}{3}\frac{\Phi_0}{h}\left(S_1U+S_2V+S_3W\right)=0, \tag{48}$$

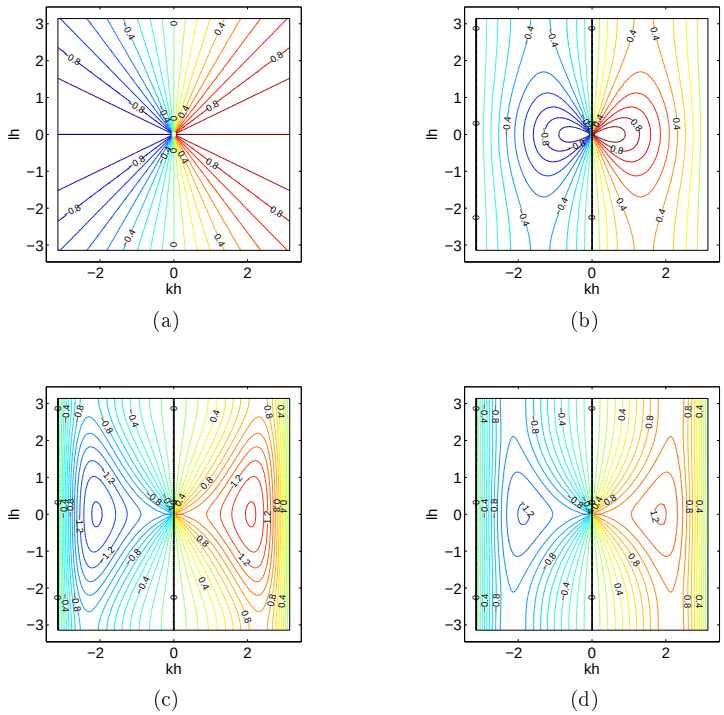

Figure 11: Normalised group velocity for the gravity-wave equations: (a) Exact solution (b) C-grid finite difference, (c) non-compound quadrilateral RT_0 element and (d) compound quadrilateral $RT0$ element. Solid black lines indicate the zero contour. All plots show the $x-$component of group velocity, the $y-$component can be obtained by rotation of -90 degrees. Contour interval 0.1.

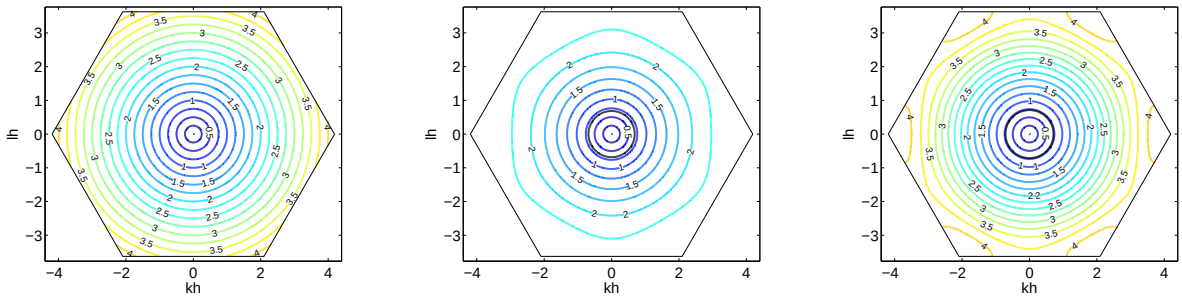

Figure 12: Normalised $\left(\omega h/\sqrt{\Phi_0}\right)$ dispersion relation for gravity-wave equations ($f \equiv 0$): (a) Exact solution, (b) C-grid finite difference, (c) compound hexagonal RT_0 element. Contour interval 0.25. Solid black contour shows the effective resolution, the region within which the dispersion relation error $\leq 1\%$.

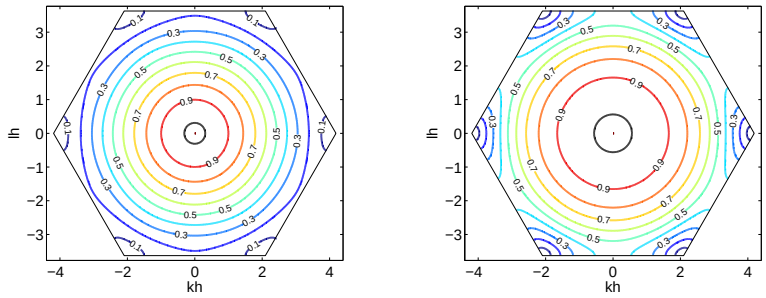

Figure 13: Normalised (ω/f) dispersion relation for inertia-wave equations ($\Phi_0 \equiv 0$): (a) C-grid finite difference, (b) compound hexagonal RT_0 element. Contour interval 0.1. Solid black contour shows the effective resolution, the region within which the dispersion relation error $\leq 1\%$.

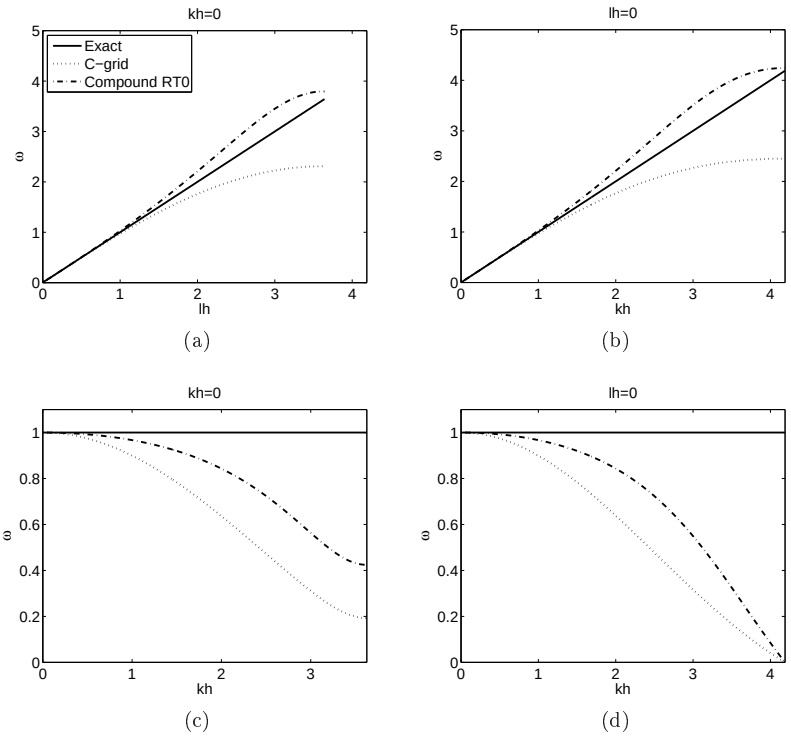

Figure 14: Hexagonal elements: (a) & (c) Centroid-edge ($kh = 0$) and (b) & (d) Centroid-node ($lh = 0$) cross-sections of the gravity wave (a-b) and inertia-wave (c-d) limits.

$$\omega\left[\overline{C}_1U+\widetilde{C}_3V+\widetilde{C}_2W\right]+2S_1\frac{P}{h}+\left(\widehat{C}_3V-\widehat{C}_2W\right) = 0, \tag{49}$$

$$\omega\left[\overline{C}_2V+\widetilde{C}_1W+\widetilde{C}_3U\right]+2S_2\frac{P}{h}+\left(\widehat{C}_1W-\widehat{C}_3U\right) = 0, \tag{50}$$

$$\omega\left[\overline{C}_3W+\widetilde{C}_2U+\widetilde{C}_1V\right]+2S_3\frac{P}{h}+\left(\widehat{C}_2U-\widehat{C}_1V\right) = 0. \tag{51}$$

with

$$\widetilde{C}_p \equiv -\frac{1}{108}\left(-28C_qC_r+10C_p\right), \tag{52}$$

$$\widehat{C}_p \equiv \frac{i}{3\sqrt{3}}f\left(2C_qC_r+C_p\right), \tag{53}$$

$$\overline{C}_p = -\frac{1}{108}\left(50+40C_p^2\right) \tag{54}$$

where $p=1,2,3$ and q,r are cyclic increments of p and q respectively. Writing (48)-(51) in matrix form gives

$$\begin{bmatrix} -\omega & \frac{4}{3}\frac{\Phi_0}{h}S_1 & \frac{4}{3}\frac{\Phi_0}{h}S_2 & \frac{4}{3}\frac{\Phi_0}{h}S_3 \\ \frac{2S_1}{h} & \omega\overline{C}_1 & \omega C_3+\widehat{C}_3 & \omega C_2-\widehat{C}_2 \\ \frac{2S_2}{h} & \omega\widetilde{C}_3-\widehat{C}_3 & \omega\overline{C}_2 & \omega\widetilde{C}_1+\widehat{C}_1 \\ \frac{2S_3}{h} & \omega\widetilde{C}_2+\widehat{C}_2 & \omega\widetilde{C}_1-\widehat{C}_1 & \omega\overline{C}_3 \end{bmatrix}\begin{bmatrix} P \\ U \\ V \\ W \end{bmatrix} = \mathbf{0}. \tag{55}$$

This can be solved to give the dispersion relation (which is omitted for brevity). There are four roots corresponding to two inertia-gravity waves solutions and two Rossby modes (one of which is spurious, as with the C-grid discretisation due to the 3:1 velocity to geopotential degree of freedom ratio). For small (kh,lh) it can again be verified that

$$\omega \sim \pm 0, \pm\left\{\omega_0+\frac{1}{288\omega_0}\left(k^2+l^2\right)\left[8\Phi_0\left(k^2+l^2\right)-9f^2\right]h^2+O(h^4)\right\}, \tag{56}$$

with $\omega_0=\sqrt{\Phi_0\left(k^2+l^2\right)+f^2}$ as before, providing a useful check on the correctness of (55) and showing that, as with the quadrilateral elements, the scheme is second order accurate on regular grids. Again the presence of the $\omega=0$ root is guaranteed by the mimetic properties of the scheme. The second zero root is the computational Rossby mode that due to the f-plane approximation made here degenerates to a zero frequency mode. Thuburn (2008) analysed the impact of this extra root in the dispersion relation and Thuburn *et al.* (2013) investigate the impact of it on a numerical simulation showing that if the potential vorticity advection is well handled then the computational mode has little effect.

For pure gravity waves ($f\equiv 0$) the positive non-zero root of (55) is shown in Fig. 12 along with the exact and C-grid finite difference results for comparison. The limits of the domain are given by the first Brillouin zone of the hexagonal lattice and can be practically determined by observing where the dispersion relation starts to repeat itself; the wavenumber ranges are $lh\in\left(-\frac{2}{\sqrt{3}}\pi,\frac{2}{\sqrt{3}}\pi\right)$ and $kh\in\left(-\frac{4}{3}\pi+\frac{|lh|}{\sqrt{3}},\frac{4}{3}\pi-\frac{|lh|}{\sqrt{3}}\right)$. Both the compound RT_0 and C-grid discretisations show improved isotropy compared with the equivalent quadrilateral discretisations, and again this is improved in the compound element case compared with the C-grid. Cross-sections of Figs 12 and 13 along centroid-edge and centroid-node slices are shown in Fig 14. In common with both the standard and compound quadrilateral elements, the compound hexagonal element overestimates the frequency for large wavenumbers for gravity waves compared with the C-grid which underestimates the frequency. However, the estimation error in the compound element is smaller as can be seen from the compound dispersion relation lying closer to the exact solution. As with the quadrilateral elements, the compound RT_0 elements exhibit spuriously high frequency waves, though this is much reduced compared with the quadrilateral elements, as shown in Table 2.

For pure inertia waves ($\Phi_0\equiv 0$) the positive non-zero roots are shown in Fig. 13, again along with the C-grid finite difference results for comparison. In this case the exact solution is unity and so is not shown.

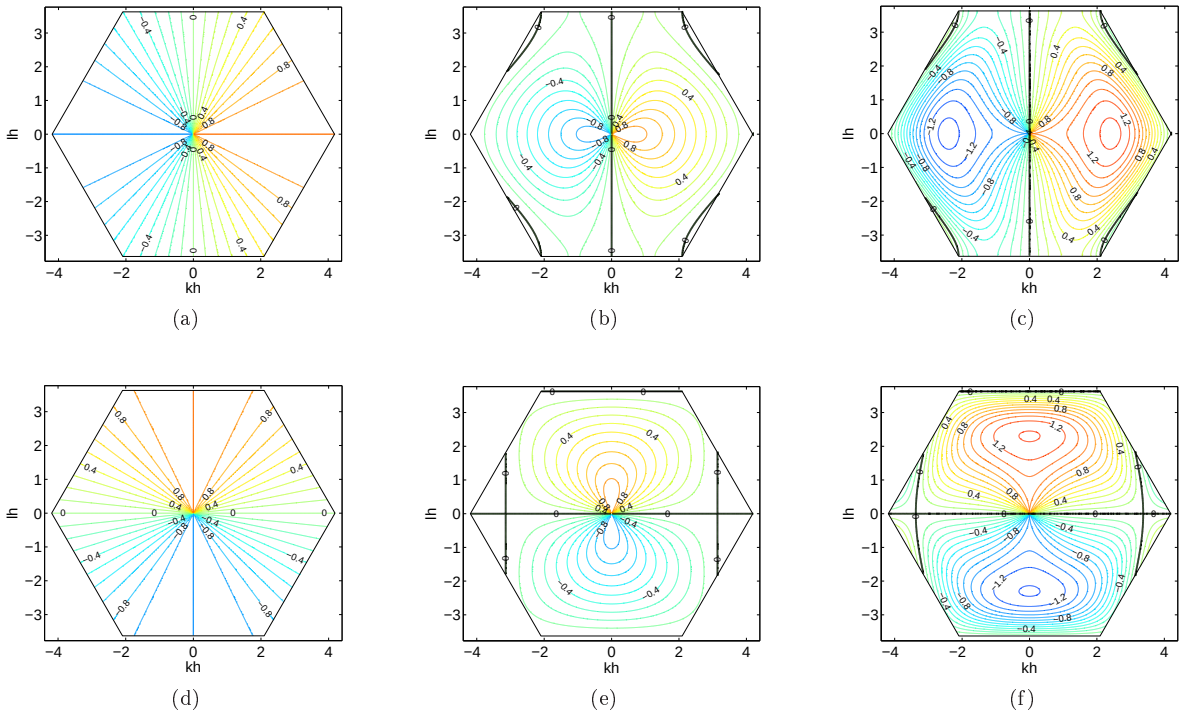

Figure 15: Normalised group velocity for the gravity-wave equations: (a)-(c) x-component & (d)-(f) y-component, with (a) & (d) exact solution, (b) & (e) C-grid finite difference and (c) & (f) compound hexagonal RT_0 element. Solid black lines indicate the zero contour. Contour interval 0.1.

Scheme	$\omega_{max}^{num}/\omega_{max}^{exact}$
Quad C-grid	0.6366
Quad RT_0	1.103
Compound Quad RT_0	1.103
Hex C-grid	0.585
Compound Hex RT_0	1.012

Table 2: Ratio of maximum numerical frequency to maximum exact frequency $\omega_{max}^{num}/\omega_{max}^{exact}$ for the gravity wave equations with quadrilateral and hexagonal elements. These maxima occur at the corners of the plots in figures 8 and 12, that is at $kh = lh = \pm\pi$ for the quadrilateral elements and at $k_j h = 4\pi/3$ for hexagonal elements where $j = 1$ or 2 or 3 and k_j is given by one of (47).

Scheme	Effective resolution $\varepsilon = 0.01$		Effective resolution $\varepsilon = 0.1$	
	Gravity Waves	Inertia Waves	Gravity Waves	Inertia Waves
Quadrilateral C-Grid	$10.1h$	$22.20h$	$4.65h$	$6.97h$
Quadrilateral RT_0	$10.47h$	$13.02h$	$4.7h$	$4.50h$
Quadrilateral Compound RT_0	$9.15h$	$14.46h$	$4.14h$	$4.88h$
Hexagonal C-Grid	$9.17h$	$20.27h$	$4.22h$	$6.30h$
Hexagonal Compound RT_0	$8.83h$	$11.21h$	$4.07h$	$3.80h$

Table 3: Effective resolution for gravity-wave and inertia-wave dispersion with error levels $\varepsilon = 0.01, 0.1$ of the different spatial discretisations.

As with the quadrilateral elements, there is less difference between the discretisations for the inertia-wave limit, but again the compound element frequency decays more slowly than the C-grid. In contrast with the gravity wave case both the compound and C-grid methods underestimate the frequency, although again the error for the compound element is smaller than the C-grid.

The $x-$ and $y-$components of the group velocity are shown in Fig. 15. Again the compound elements show a spurious speeding up of some waves with $\text{Max}\,(C_g) \approx 1.3$, occurring at $(kh, lh) \approx (2.42, 0)$. In contrast with the quadrilateral elements there are now small regions of wavenumber space where a component of the group velocity vector spuriously changes sign for both the C-grid and RT_0 discretisations, this means that wavepackets in these regions will have a component in either the x or y direction that travels in the wrong direction. These regions are however both small in extent and at the limits of the resolvable resolution, in addition the magnitude of the group velocity in these regions is small and so the effect on the accuracy of the model is likely to be small, c.f. a collocated A-grid method where (in 1-dimension) half the spectrum has the wrong sign of group velocity and of up to the same magnitude as the exact solution. Additionally since these regions of negative group velocity are for small scale waves and since nonlinear models generally dissipate on the small scales this will likely further reduce the impact of these regions of negative group velocity.

5.3 Effective Resolution

To try to quantify the accuracy of the numerical schemes at approximating the continuous equations the effective resolution of each discretisation is computed. The effective resolution is defined to be the resolution at which the numerical scheme can be considered to have accurately resolved the flow. To quantify this, the definition of Ullrich (2014) is used: for a given error level ε, the shortest resolved wavelength λ is some multiple of the grid spacing $\lambda = bh$ such that

$$\left| \frac{h}{\sqrt{\Phi_0}} \left(\omega_{numerical} - \omega_{exact} \right) \right| \leq \varepsilon. \tag{57}$$

For $\varepsilon = 0.01$ and $\varepsilon = 0.1$, which correspond to the numerical solution being within 1% and 10% respectively of the exact solution, the effective resolutions for the different schemes are listed in Table 3. These are obtained numerically from Figures 8, 9, 12 and 13 by finding the point at which the inequality (57) fails to hold. This shows that for pure gravity waves there is a small increase in accuracy (of the order $h/2 - h$) from using the compound elements. For pure inertia waves the improvement over the C-grid methods is much greater, but for quadrilaterals the effective resolution when using compound elements is actually slightly worse than with non-compound elements. The effective resolution contour corresponding to $\varepsilon = 0.01$ is also shown in Figs. 8-9 and 12-13 as a solid black line, where the more isotropic nature of the compound quadrilateral elements and the hexagonal methods can be seen.

5.4 Variable Rossby radius

So far all the results presented have been for the two ends of the inertia-gravity wave spectrum, either pure gravity waves ($f \equiv 0$) or pure inertia waves ($\Phi_0 \equiv 0$). However, in practice we are interested in the

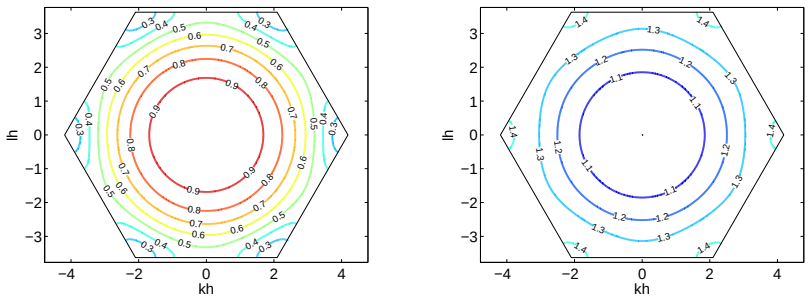

(a) $R_d/h = 1/20$ (b) $R_d/h = 1/3$

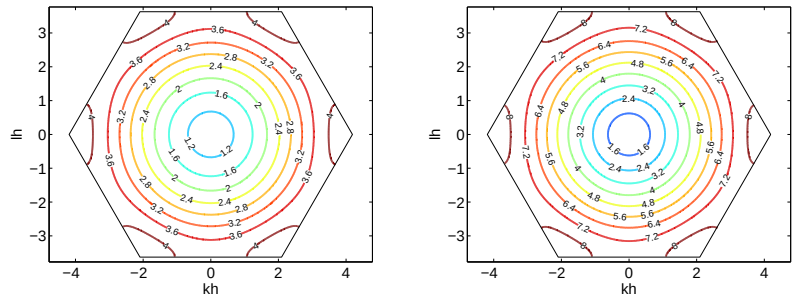

(c) $R_d/h = 1$ (d) $R_d/h = 2$

Figure 16: Normalised dispersion relation (ω/f) for hexagonal compound elements with a variably resolved Rossby radius, ranging from $R_d/h = 1/20$ (coarse resolution) to $R_d/h = 2$ (well resolved).

propagation of mixed inertia-gravity waves for a range of values of the Rossby radius $R_d = \sqrt{\Phi_0}/f$. Following Le Roux (2012) four values of the normalised Rossby radius are chosen $R_d/h = 1/20, 1/3, 1, 2$ ranging from a coarse resolution $R_d/h = 1/20$ of the Rossby radius up to a well resolved radius $R_d/h = 2$. The dispersion relation for the hexagonal compound element is shown in Figure 16 and 1D slices along $lh = 0$ for both the hexagonal compound elements and C-grid discretisation are shown in 17. In common with the earlier results when the Rossby radius is well resolved the compound elements accurately represent the dispersion relation whilst for poorly resolved wavenumbers the representation is less good as was found with pure inertia waves. However compared with the C-grid discretisation the compound elements do a much better job for moderately resolved Rossby waves $R_d/h = 1/3, 1$. A similar representation is found for the quadrilatetral elements (not shown).

6 Numerical Simulations

To test the theoretical predictions of the previous sections numerical integrations are performed. The question we are primarily interested in answering is what is the effect of the small improvement in the dispersion properties predicted by the previous analysis? Additionally, we are interested if there is any significant change in the accuracy of the model and finally whether any of the improvement to the dispersion properties that were analysed on a uniform Cartesian mesh carry over to a quasi-uniform spherical mesh. For a more general discussion of the performance of these methods on a standard set of spherical shallow water test cases the interested reader if referred to Thuburn *et al.* (2013) and Thuburn and Cotter (2015).

To perform the numerical integrations a centred semi-implicit time discretisation is used. Equations (26) and (27) can be combined, yielding

$$A^{+}\mathbf{y}^{n+1} = A^{-}\mathbf{y}^{n}, \tag{58}$$

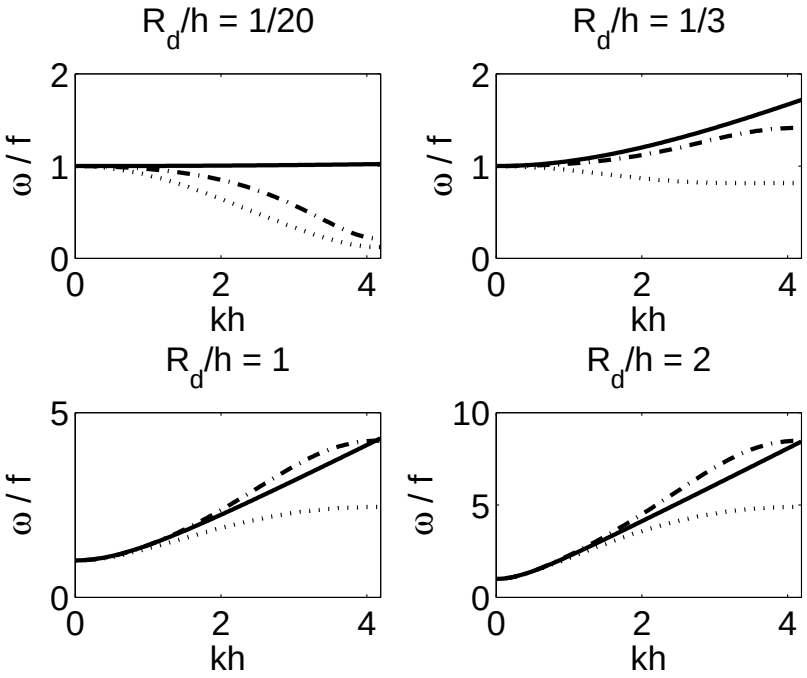

Figure 17: 1D slices of the dispersion relation at $lh = 0$ for hexagonal compound elements with a variably resolved Rossby radius, ranging from $R_d/h = 1/20$ (coarse resolution) to $R_d/h = 2$ (well resolved). The exact solution is shown by a solid line, the compound elements with a dash-dotted line and the C-grid solution with a dotted line.

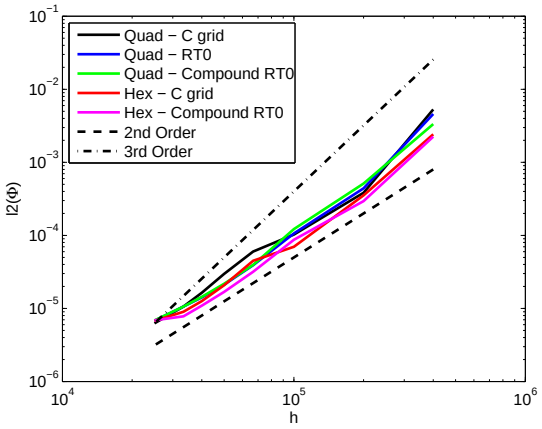

Figure 18: $l_2(\Phi)$ error for the compound and standard RT_0 elements as well as a C-grid scheme for both quadrilateral and hexagonal elements.

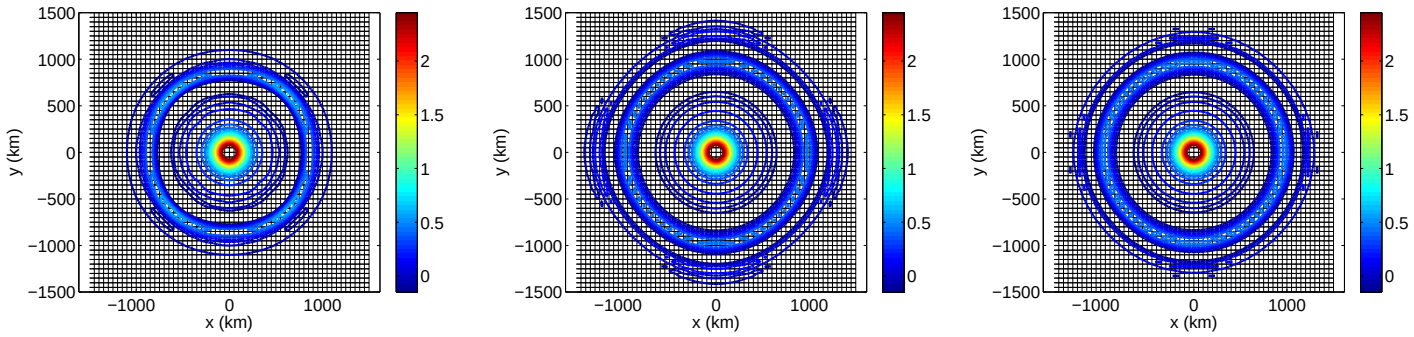

(a) (b) (c)

Figure 19: Goepotential profiles for numerical integration using a centred implicit timestepping method for (a) quad C-grid, (b) quad RT_0 elements and (c) quad compound RT_0 elements. Contour intervals $0.1\,\mathrm{m}^2/\mathrm{s}^2$.

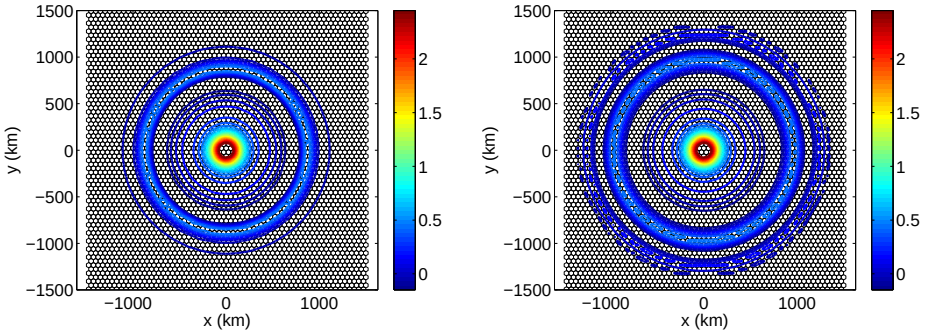

(a) (b)

Figure 20: Goepotential profiles for numerical integration using a centred implicit timestepping method for (a) hexagonal C-grid and (b) hexagonal compound RT_0 elements. Contour intervals $0.1\,\mathrm{m}^2/\mathrm{s}^2$.

where $\mathbf{y} = \left[\hat{\Phi}, \hat{u}\right]^T$ and

$$A^{\pm} \equiv \begin{bmatrix} M_\Phi & \pm\frac{\Delta t}{2}\Phi_0 D \\ \mp\frac{\Delta t}{2}D^T & M_u \pm \frac{\Delta t}{2}F \end{bmatrix}. \tag{59}$$

The components of the system matrix $A^{\pm}$ for a uniform orthogonal grid are given in Appendix A. Due to the small size of problems investigated here the system of equations (58) is solved exactly using Guassian elimination, but for larger problems a iterative solver such as Congjugate gradient could instead be used.

6.1 Uniform elements

To test the convergence of the numerical scheme equation (58) is initialised with a steady state analytical solution defined via the streamfunction

$$\psi\left(\mathbf{x}, t=0\right) = \psi_0 \exp\left(-\frac{x^2+y^2}{a^2}\right). \tag{60}$$

The balanced velocity field is therefore

$$\mathbf{u}\left(\mathbf{x}, t=0\right) = \nabla^{\perp}\psi\left(\mathbf{x}, t=0\right), \tag{61}$$

and the supporting initial geopotential field is given by

$$\Phi(\mathbf{x}, t=0) = f\psi(\mathbf{x}, t=0). \tag{62}$$

This initial condition is integrated for a period of 10 days on a uniform domain of size $3000\,km \times 3000\,km$ for different resolutions. A timestep of $\Delta t = 600$ s is used. Note we are primarily interested in effects of the space discretisation but the choice of time discretisation would also be expected to have some small influence on the results in Figs. 19 and 20; to avoid this the timestep has been chosen suitably small so that the temporal errors are small and as a check, reducing the timestep further by a factor of 10 produces no visible difference to the results. The constants $\psi_0 \equiv \Phi_0 = 10^2\,\mathrm{m}^2/\mathrm{s}^2$ and $f = 10^{-4}\,\mathrm{s}^{-1}$, $a = 4 \times 10^5\,\mathrm{m}$. The convergence of the $l_2(\Phi)$ error for each scheme with various element widths in the range $h = 25 - 400\,\mathrm{km}$ is shown in Fig. 18. All schemes show the second-order convergence expected on a regular grid with the hexagonal based methods exhibiting a slightly smaller coefficient. (Note, however, that on nonuniform grids these methods are all, at best first-order).

The dispersion properties can be observed by removing the support of the initial velocity field, $\mathbf{u}(\mathbf{x}, t=0) = 0$, from the initial state (62) along with reducing the width of the Gaussian (60) to $a = 2h$. Integrations are performed with a constant element width $h = 50\,k$m and run until $t = 30$ hours. The unsupported initial Φ field projects energy onto a wide spectrum of inertia-gravity waves that propagate radially from the central perturbation according to the appropriate dispersion relation. The final Φ profiles are shown in Fig. 19 for the quadrilateral elements and Fig. 20 for the hexagonal elements. The effects of the increase in the group velocity for a given wavenumber k, compared to the exact value $C_g = \frac{\Phi_0 k}{\sqrt{\Phi_0 k^2 + f^2}}$, for the RT_0 discretisations can clearly be seen from the location of the outermost contours particularly in contrast with the decrease in the group velocity for the C-grid schemes. The greater isotropy of the compound quadrilateral elements can also be seen in the marginally more circular contours of Fig. 19 (c) compared with the other discretisations. In contrast the hexagonal C-grid finite difference scheme is already very isotropic, so the differences observed in the hexagonal elements, Fig. 20 (b) are much smaller.

6.2 Spherical domains

To compare the performance of the compound element method with a standard finite volume C-grid method in a more realistic setting, the compound element model of Thuburn and Cotter, 2015 is compared with the finite volume model of Thuburn *et al.*, 2013 on both cubed sphere grids and icosahedral grids. Both models simulate the nonlinear shallow water equations on the sphere using a mimetic discretisation with semi-implicit time stepping and swept area forward in time advection schemes on both the primal and dual grid. The convergence and accuracy of the various schemes considered here are discussed in some detail in Thuburn *et al.*, 2013, for the C-grid schemes, and Thuburn and Cotter, 2015 for the compound element schemes, in the context of quasi-uniform spherical grids and the interested reader is referred to these papers for more details. The icosahedral mesh is generated following Heikes and Randall (1995a,b) (but without the twist) and the cubed sphere is based upon the equi-angular cubed sphere of Ronchi *et al.* (1996) but with a single step of the smoothing described in Thuburn *et al.* (2013). The application of the compound finite element method to these spherical grids is presented in Thuburn and Cotter (2015) and the interested reader is referred there. To mimic the planar dispersion test of Section 6.1 the geopotential field is initialised with a Gaussian perturbation and the initial wind field is set to zero

$$\Phi(\lambda, \phi, t=0) = \Phi_0 \left\{ 1 + \frac{1}{10} \exp\left[-\left(\frac{r}{a}\right)^2 \right] \right\}, \tag{63}$$

$$\mathbf{u}(\lambda, \phi, t=0) = 0, \tag{64}$$

with

$$r = \cos^{-1}\left[\sin\phi_0 \sin\phi + \cos\phi_0 \cos\phi \cos(\lambda - \lambda_0) \right], \tag{65}$$

the great circle distance on a unit sphere from the point $(\lambda_0, \phi_0) = (4\pi/5, \pi/4)$, the perturbation half-width is $a = 1/25$ and $\Phi_0 = 10^2\,\mathrm{m}^2/\mathrm{s}^2$. The test is run on a non-rotating sphere for 12 hours with a timestep of $\Delta t = 112.5$ s. The results, using both a high resolution (221184 faces) cubed-sphere and lower resolution cubed-sphere (3456 faces) and icosahedral (2562 faces), are shown in Figure 21. As with the planar results

the most obvious difference between the compound elements and the finite volume results is the speed of wave propagation. Compared to the high resolution results the bulk of the wave in the finite volume methods has been retarded, such that there are still a number of contours close to the initial location of the wave, whilst the finite element method has sped the wave front up. To ease comparison of the propagation speed a great circle line has been added to each figure corresponding to the leading edge of the high resolution solution. In contrast to the planar results it is very difficult to observe any increased circular symmetry in the compound element results compared with the equivalent finite volume ones and it is likely that any potential slight improvement has been hidden by the larger scale errors caused by using a non-uniform-non-orthogonal grid, and the added complexity of the nonlinear terms. As with the previous results the hexagonal grid methods generally produce better results showing better symmetry in the resulting wave form even though they are being nominally run at a lower resolution ($\sim 75\%$ of the number of cells as the cubed-sphere runs), though, due to the extra velocity points there are approximately the same number of total degrees of freedom on the two grids.

6.3 Computational Cost

The computational cost of the compound element method compared to other methods is hard to analyse as it is dependent upon the particular application, implementation and architecture being used. Nevertheless a broad outline of some of the potential costs can be given. For the method used here, the computational cost mainly consists of constructing the matrices M_Φ, M_u, D, F and inverting the A^+ matrix. Since all of these matrices are constant in time they can be computed once at set up and then stored. This method is the same for all the numerical schemes considered here with the added simplification that for the C-grid methods the velocity mass matrix (M_u) is diagonal. Since the matrices are precomputed the only additional cost of using the compound element method is to compute the element matrices, which involves applying the conditions in Section 3 to each sub-element. As this is a one-off setup cost it means that the computational cost of each method is similar.

For a more complicated application, such as for the nonlinear shallow water equations or 3D Euler equations equations it may become impractical to precompute and store a large number of operators at high resolution (though this is exactly what is done in Thuburn and Cotter (2015)). In which case, if the quadrature is performed on the fly, then each evaluation of a field on the grid will involve evaluation at quadrature points for all the sub-elements of each element instead of just the full element, i.e for a quadrilateral compound element it would be necessary to compute functions in each of the 8 triangular sub-elements instead of just the single quadrilateral element as for the standard RT0 implementation. In broad terms the number of floating point operations for evaluating a function on a grid of n cells will rise from n evaluations on a quadrilateral/hexagonal element to $8n$ or $12n$ evaluations on triangular elements for a quadrilateral or hexagonal grid. This cost will be somewhat mitigated by the smaller number of operations e.g fewer quadrature points needed for evaluation on a triangular element.

7 Conclusions

The discrete harmonic extension method of Christiansen (2008) has been used to build polygonal compound RT_0 elements from a number of triangular sub-elements, such that the primal and dual grid elements are constructed from the same sub-elements. It was found that even for uniform quadrilateral elements the obtained discretisation differs from the standard RT_0 discretisation and inherits elements of the underlying triangular geometry. For the linear shallow water equations considered here only two compound function spaces $\mathbb{V}_1$, $\mathbb{V}_2$ are required and so the construction of the third space $\mathbb{V}_0$ has not been documented, though the same method can be applied, see also Thuburn and Cotter (2015).

The dispersion properties of the compound elements in both the gravity- and inertia-wave asymptotic limits have been investigated and compared with the well-known C-grid discretisations on uniform hexagonal grids and with both the C-grid and non-compound RT_0 elements on uniform quadrilateral grids. The compound elements are found to have a more isotropic dispersion relation, which is most noticeable on a quadrilateral grid and improves upon the standard C-grid and RT_0 methods. Additionally, on quadrilaterals, the overshoots in the dispersion relation for high frequency waves with the RT_0 elements, that manifests themselves as spuriously fast moving waves, have been significantly reduced. The compound hexagonal

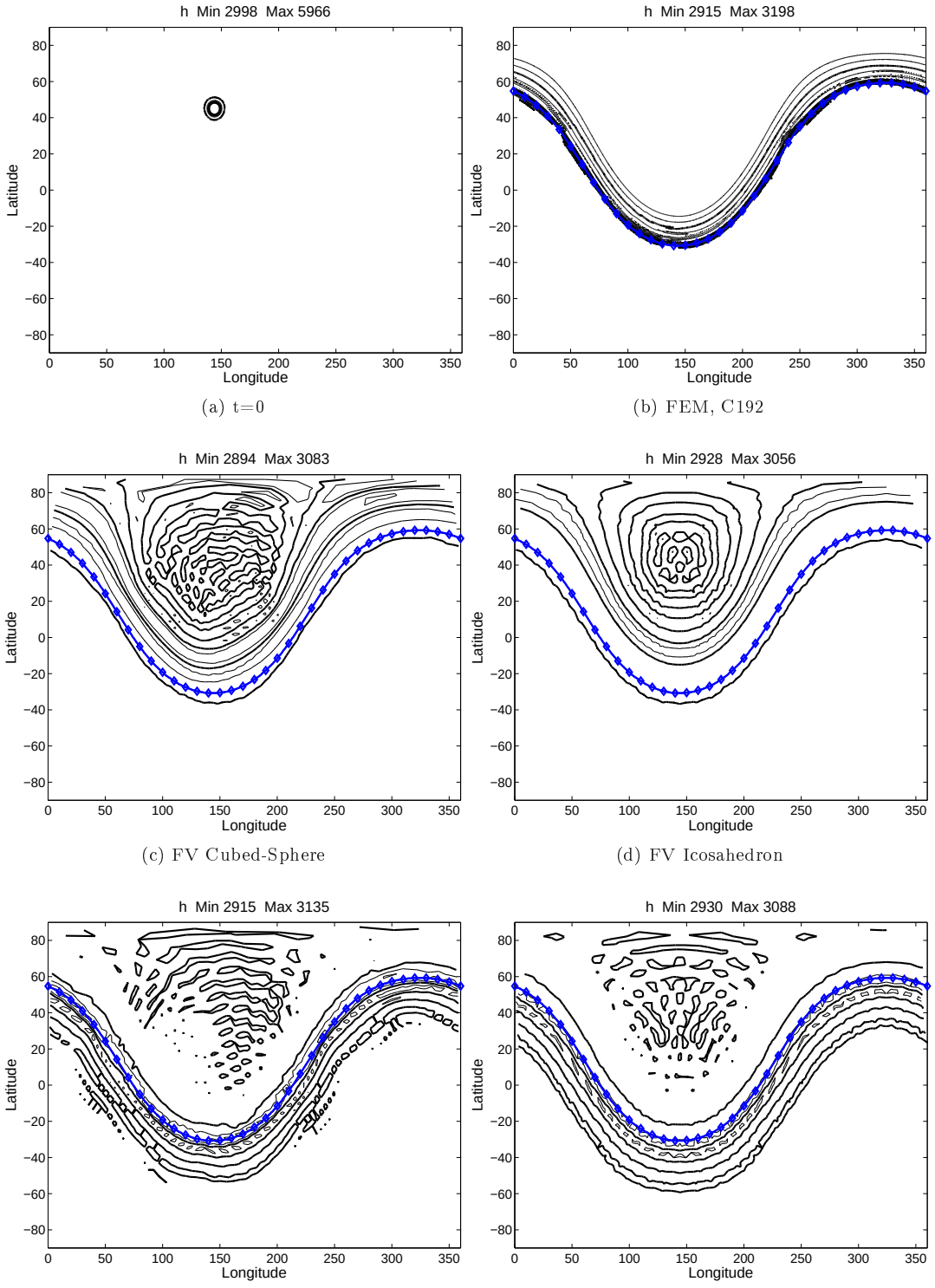

(a) t=0

(b) FEM, C192

(c) FV Cubed-Sphere

(d) FV Icosahedron

(e) FEM cubed-sphere

(f) FEM Icosahedron

Figure 21: Evolution of a narrow Gaussian hill using finite volume and compound finite element methods on spherical grids. (a) Initial height profile on high resolution cubed sphere (221184 faces) (b) Final height profile on high resolution cubed sphere (221184 faces) using compound finite elements. Final height profiles on (c) cubed sphere grid (3456 faces) and (d) icosahedral grid (2562 faces) using a finite volume method. Final profiles with compound finite element methods on cubed sphere (e) and icosahedral grids (f) at the same resolution as (c) & (d). In all plots Contour intervals are every 50 m, and every 100 m is shown in a bold line. For comparison a great circle line located at the front of the high resolution wave is shown with diamond markers.

elements again have a more isotropic dispersion relation than the C-grid equivalent, though the difference here is less marked. In comparison with the C-grid, the compound element is more accurate for large wave numbers with a slight overestimation of the frequency compared with a large underestimation. Comparing the finite volume and finite elements in a more complicated spherical gravity-wave dispersion test the leading order difference is the propagation speed of poorly resolved waves and any increased isotropy of the finite element method is much harder to detect.

The benefits of these compound elements have to be weighed against the increased cost associated with a denser mass matrix for the momentum equation, (A.5) & (A.9) even on an orthogonal grid where the u and v velocity components would not normally be expected to couple. This cost can be lessened when using an implicit scheme due to the need to invert a system matrix, of which the mass matrix forms but a part. In addition the cost of computing the reduction from the sub-element stencil to the compound element one must be included, but for a time independent grid this can be included as a one-off pre-processing cost.

Compound elements provide a way of constructing compatible finite element spaces on general polygonal grids, such as hexagons, as well as primal and dual families of compatible finite element spaces, and thus broaden the options available for developing geophysical models with desirable conservation and balance properties. We have demonstrated here another advantage of compound elements, which is that their wave dispersion properties are as good as, and in nearly all cases a small improvement on, those of analogous finite difference or standard finite element schemes.

Acknowledgments

The authors would like to thank Daniel Le Roux and two anonomous reviewers for their helpful suggestions on how to improve the paper and also Nigel Wood for comments on an early draft of the paper. The work of John Thuburn was funded by the Natural Environment Research Council under the "Gung Ho" project (grant NE/1021136/1).

References

Arakawa A, Lamb VR. 1977. Computational design of the basic dynamical processes of the UCLA general circulation model. *Methods in Comp. Phys.* **17**: 174–265.

Auricchio F, Brezzi F, Lovadina C. 2004. *Mixed finite element methods.* John Wiley. DOI:10.1002/0470091355.ecm004.

Buffa A, Christiansen S. 2007. A dual finite element complex on the barycentric refinement. *Math. Comp.* **76**: 1743–1769.

Christiansen S. 2008. A construction of spaces of compatible differential forms on celluar complexes. *Math. Models and Meth. in App. Sci.* **18**: 739–758.

Cotter CJ, Shipton J. 2012. Mixed finite elements for numerical weather prediction. *J. Comput. Phys.* **231**: 7076–7091.

Cotter CJ, Thuburn J. 2014. A finite element exterior calculus framework for the rotating shallow-water equations. *J. Comp. Phys.* **257**: 1506–1526.

Coxeter HSM (ed). 1989. *Introduction to geometry.* Wiley. 2nd edition.

Danilov S. 2010. On the utility of triangular C-grid type discretization for numerical modeling of large-scale ocean flows. *Ocean Dynamics* **60**: 1361–1369.

Gassmann A. 2013. A hexagonal non-hydrostatic C-grid dynamical core. *Quarterly Journal of the Royal Meteorological Society* **139**: 152–175.

Heikes R, Randall DA. 1995a. Numerical integration of the shallow-water equations on a twisted icosahedral grid. Part I: basic design and results of tests. *Mon. Wea. Rev.* **123**: 1862–1880.

Heikes R, Randall DA. 1995b. Numerical integration of the shallow-water equations on a twisted icosahedral grid. Part II: a detailed description of the grid and an analysis of of numerical accuracy. *Mon. Wea. Rev.* **123**: 1881–1887.

Le Roux DY. 2012. Spurious inertial oscillations in shallow-water models. *J. Comput. Phys.* **231**: 7959–7987. DOI:10.1016/j.jcp.2012.04.052.

Le Roux DY, Rostand V, Pouliot B. 2008. Analysis of numerically induced oscillations in 2d finite-element shallow-water models Part II: Free planetary waves. *SIAM J. Sci. Comput.* **30**: 1970–1991.

Majewski D, Liermann D, Prohl P, Ritter B, Buchhold M, Hanisch T, Paul G, Wergen W, Baumgardner J. 2002. The operational global icosahedral-hexagonal gridpoint model GME: Description and high-resolution tests. *Mon. Wea. Rev.* **130**: 319–338.

Melvin T, Staniforth A, Thuburn J. 2012. Dispersion analysis of the Spectral Element Method. *Q. J. R. Meteorol. Soc.* **138**: 1934–1947.

Raviart P, Thomas J. 1977. A mixed finite element method for 2nd order elliptic problems. In: *Mathematical Aspects of Finite Element Methods*, Galligani I, Magenes E (eds). Springer-Verlag, pp. 292–315.

Ronchi C, Iacono R, Paolucci P. 1996. The cubed sphere: A new method for the solution of partial differential equations in spherical geometry. *J. Comput. Phys.* **124**: 93–114.

Satoh M, Matsuno T, Tomita H, Miura H, Nasuno T, Iga S. 2008. Nonhydrostatic icosahedral atmospheric model (NICAM) for global cloud resolving simulations. *J. Comput. Phys.* **227**: 3486–3514.

Skamarock W, Klemp J, Duda M, Fowler L, Park SH, Ringler T. 2012. A multiscale nonhydrostatic atmospheric model using centroidal Voronoi tesselations and C-grid staggering. *Mon. Wea. Rev.* **140**: 3090–3105.

Staniforth A, Melvin T, Cotter C. 2013. Analysis of a mixed finite-element pair proposed for an atmospheric dynamical core. *Q. J. R. Meteorol. Soc.* **139**: 1239–1254. DOI:10.1002/qj.2028.

Staniforth A, Thuburn J. 2012. Horizontal grids for global weather prediction and climate models: a review. *Q. J. R. Meteorol. Soc.* **138**: 1–26.

Taylor MA, Fournier A. 2010. A compatible and conservative spectral element method on unstructured grids. *J. Comput. Phys.* **229**: 5879–5895.

Thuburn J. 2008. Numerical wave propagation on the hexagonal C-grid. *J. Comput. Phys.* **227**: 5836–5858.

Thuburn J, Cotter CJ. 2015. A primal-dual mimetic finite element scheme for the rotating shallow water equations on polygonal spherical meshes. *J. Comp. Phys.* **290**: 274–297.

Thuburn J, Cotter CJ, Dubos T. 2013. Mimetic, semi-implicit, forward-in-time, finite volume shallow water model: comparison of hexagonal-icosahedral and cubed sphere grids. *GMDD* **6**: 6867–6925.

Ullrich PA. 2014. Understanding the treatment of waves in atmospheric models, Part I: The shortest resolved waves of the 1D linearized shallow water equations. *Q.J.R. Meteorol. Soc.* **140**: 1426–1440. DOI:10.1002/qj.2226.

Ullrich PA, Jablonowski C, van Leer B. 2010. High-order finite-volume methods for the shallow-water equations on the sphere. *J. Comput. Phys.* **229**: 6104–6134.

A Element Matrices

The matrix operators for a single element/cell on a uniform grid are given here for quadrilateral and hexagonal elements where the element width is h

A.1 Quadrilateral Elements

For the continuity equation the mass matrix is the 1x1 matrix

$$M_\Phi \equiv h^2, \tag{A.1}$$

the divergence operator is

$$D \equiv h \left[\begin{array}{cccc} 1, & -1, & 1, & -1 \end{array} \right]^T, \tag{A.2}$$

and the Coriolis matrix is

$$F \equiv \frac{fh^2}{4} \begin{bmatrix} 0 & 0 & -1 & -1 \\ 0 & 0 & -1 & -1 \\ 1 & 1 & 0 & 0 \\ 1 & 1 & 0 & 0 \end{bmatrix}. \tag{A.3}$$

The momentum mass matrix differs, depending upon the discretisation (C-grid, RT_0, compound RT_0), For a C-grid discretisation the mass matrix is the appropriate identity matrix, $h^2 I_4$. For a regular quadrilateral RT_0 element the mass matrix is

$$M_u \equiv \frac{h^2}{6} \begin{bmatrix} 2 & 1 & 0 & 0 \\ 1 & 2 & 0 & 0 \\ 0 & 0 & 2 & 1 \\ 0 & 0 & 1 & 2 \end{bmatrix}, \tag{A.4}$$

whilst for a compound RT_0 element it is

$$M_u \equiv \frac{h^2}{48} \begin{bmatrix} 17 & 7 & -1 & 1 \\ 7 & 17 & 1 & -1 \\ -1 & 1 & 17 & 7 \\ 1 & -1 & 7 & 17 \end{bmatrix}. \tag{A.5}$$

A.2 Hexagonal Elements

For the continuity equation the mass matrix is again a 1x1 matrix

$$M_\Phi \equiv \frac{\sqrt{3}}{2} h^2, \tag{A.6}$$

the divergence operator is

$$D \equiv \frac{h}{\sqrt{3}} \left[\begin{array}{cccccc} 1, & -1, & 1, & -1, & 1, & -1 \end{array} \right]^T, \tag{A.7}$$

and the Coriolis matrix is

$$F \equiv \frac{h^2 f}{18} \begin{bmatrix} 0 & 0 & -1 & -2 & 1 & 2 \\ 0 & 0 & -2 & -1 & 2 & 1 \\ 1 & 2 & 0 & 0 & -1 & -2 \\ 2 & 1 & 0 & 0 & -2 & -1 \\ -1 & -2 & 1 & 2 & 0 & 0 \\ -2 & -1 & 2 & 1 & 0 & 0 \end{bmatrix}. \tag{A.8}$$

The momentum mass matrix again differs, for a C-grid discretisation the momentum mass matrix is the identity matrix, $\left(h^2/\sqrt{3}\right) I_6$. For the compound hexagonal RT_0 element mass matrix is

$$M_u \equiv \frac{h^2}{108\sqrt{3}} \begin{bmatrix} 35 & 10 & -7 & -2 & -7 & -2 \\ 10 & 35 & -2 & -7 & -2 & -7 \\ -7 & -2 & 35 & 10 & -7 & -2 \\ -2 & -7 & 10 & 35 & -2 & -7 \\ -7 & -2 & -7 & -2 & 35 & 10 \\ -2 & -7 & -2 & -7 & 10 & 35 \end{bmatrix}. \tag{A.9}$$